Effects of regional and local stress variabilities on fault slip tendency in the southern Taranaki Basin, New Zealand

Cécile Massiot[1], Hannu Seebeck[1], Andrew Nicol[2], David D. McNamara[3], Mark J. F. Lawrence[1], Angela G. Griffin[1], Glenn P. Thrasher[1], Grant O'Brien[1,*], G. Paul D. Viskovic[1]

1. GNS Science, P.O. Box 30-368, Lower Hutt 5040, New Zealand
2. Department of Geological Sciences, University of Canterbury, Christchurch 8140, New Zealand
3. Earth and Ocean Science, National University of Ireland Galway, University Road, Galway, H91 TK33, Ireland

*now at: Dam Safety Intelligence, Level 2, 33 Customhouse Quay, Wellington 6011, New Zealand

Corresponding author: Cécile Massiot, c.massiot@gns.cri.nz

Highlights:

- New borehole stress magnitude estimations and 3-D fault mapping
- Southern Taranaki Basin has a normal/strike-slip regime with ENE-WSW S_{Hmax} azimuth
- Local stress rotation near inactive seismic fault
- Favourably oriented faults but slip tendency <0.6
- Non-planar faults and local stress variations cause varied slip tendency along-fault

Keywords: stress, slip tendency, stress rotation, fault reactivation potential, southern Taranaki Basin

Abstract:

Determining the potential for faults to slip is widely employed for evaluating fault slip potential and associated earthquake hazards, and characterising hydrocarbon seal integrity and reservoir properties. Here we use borehole and 3D seismic reflection data to estimate stress orientations and magnitudes, fault geometries and slip tendency in the southern Taranaki Basin, New Zealand. Late Cenozoic normal faults in the basin range in strike from E-W to NE-SW and are associated with stress changes from basin to borehole scales. The Maui and Maari-Manaia regions, part of the eastern mobile belt, show a strike-slip/normal stress regime ($S_{Hmax} \geq S_v > S_{hmin}$). The Tui region, part of the western stable platform, shows a normal stress regime ($S_v > S_{Hmax} > S_{hmin}$). Both regions have a mean S_{Hmax} azimuth of ENE-WSW. Although the southern Taranaki basin is undergoing active deformation at plate tectonic scales, the stress magnitudes appear insufficiently high to reactivate the faults assuming a classic coefficient of friction. S_{Hmax} azimuths and S_{Hmax}:S_v magnitude ratios vary locally between boreholes and with depth. A borehole that intersects an inactive seismic-scale fault and borehole-scale faults over a 150-m interval shows S_{Hmax} to rotate by up to 30° proximal to the faults, which are favourably orientated for slip in both strike-slip and normal regimes. The small borehole-scale faults may, however, be active within the inactive seismic scale fault's damage zone. We highlight changes of slip tendency along faults resulting from local variations in the stress field and non-planar fault geometries that could not be resolved using only seismic reflection data and regional stress tensor. In the Taranaki Basin additional sub-seismic fault mapping, stress information and mechanical rock property testing are required to realise the potential of stress-based prediction of along-fault permeability and fluid migration.

1. Introduction

Tectonic and local stresses contribute to the development of structural permeability within sedimentary basins. The interactions between stress, deformation and fluid flow have become increasingly utilised for understanding fault reactivation causing potentially damaging earthquakes

and the migration of fluids in the subsurface (e.g., Barton et al., 1995; Caine et al., 1996; Sherburn and White, 2006; Zoback, 2007; Barton et al., 2009; Davatzes & Hickman, 2010; Rinaldi et al., 2014; Jolie et al., 2016; Alt & Zoback, 2017). Faults and fractures play an important role in the subsurface movement of fluids by either enhancing along-fault flow and/or impeding across-fault flow (e.g., Sibson, 1994; Aydin, 2000; Manzocchi et al., 2010, Seebeck et al., 2014a). How faults impact on the migration of fluids is dependent on a range of factors including the rock properties within and enclosing the fault, the displacement, geometry and connectivity of the fault, and the stress regime defined by the orientation and magnitude of the principal stresses acting across the fault zone (e.g., Faulkner et al., 2010; Manzocchi et al., 2010; Fig. 1). Geomechanical modelling methods, such as slip tendency analysis and dilation tendency (e.g., Morris et al., 1996; Jolie et al., 2016), have been used to predict the probability of structural permeability, and require information on the contemporary stress field together with fault geometries and fault-rock properties (e.g., strength and coefficient of friction) (e.g., Faulkner et al., 2010). Stress magnitudes are essential for these models, but can be challenging to obtain, especially the maximum horizontal stress (S_{Hmax}) which cannot be measured directly (Zoback et al., 2003; Morris & Ferrill, 2009; Heidbach et al., 2018). For such geomechanical permeability prediction techniques the underpinning theory is generally well accepted, however, it remains unclear whether available data (e.g., spatial distribution, quantity, quality and uncertainties) are sufficient to produce valuable fault-permeability predictions. Here we address this question using data from the Taranaki Basin in western offshore New Zealand (Fig. 2).

In regions which have undergone multiple episodes of deformation in varying stress fields like the southern Taranaki Basin (King & Thrasher, 1996; Reilly et al., 2015), faults are not necessarily favourably oriented for reactivation in the contemporary stress field (Sibson, 1990; Turner & Williams, 2004). The Taranaki Basin, New Zealand's only petroleum-producing basin, is actively deforming in response to oblique convergence and subduction along the Hikurangi subduction margin (King & Thrasher, 1996; Beavan et al., 2002; Reilly et al., 2015; Fig. 2). In this seismically active region, faults formed at different stages of the basin tectonic history are thought to play an

important role in both the up-sequence migration of Late Cretaceous to Eocene sourced fluids and trapping of petroleum in Paleocene to Late Miocene reservoirs (Webster et al., 2011; Hemming-Sykes, 2012; Ilg et al., 2012; Reilly et al., 2016 and references therein). Here we evaluate the contemporary stress regime in the southern Taranaki Basin to better constrain the current tectonic setting, the potential for fault slip, and its possible impact on petroleum flow in the basin.

We utilise seismic reflection surveys (2D and 3D), borehole images, conventional borehole logs and drilling data acquired by the petroleum industry, to constrain fault orientations and contemporary stress orientations and magnitudes in the southern Taranaki Basin. The available data suggest a strike-slip/normal faulting regime with local rotations in the orientation of the principal stress axes associated with nearby faults mapped from seismic reflection data. We discuss the implications of our results for modelling the slip tendency of these faults, as well as the limitations of this technique as a predictive tool for characterising fault permeability. Our analysis indicates that the models are useful for producing rupture scenarios, but that the stress estimations and fault models are unlikely to be sufficiently accurate to model fault permeability on sub-seismic scales.

2. Geological setting

The offshore southern Taranaki Basin is located between New Zealand's North and South Island's, ~400 km west of the Hikurangi subduction margin, on the eastern margin of the Australian plate (Fig. 2). The southern Taranaki Basin has experienced a complex tectonic evolution and subsidence history, leading to the accumulation of >8 km of Late Cretaceous-Recent sediments during multiple phases of extension and contraction (King & Thrasher, 1996; Reilly et al., 2015; Strogen et al., 2017). The basin initially developed during intracontinental rifting immediately prior to the break-up of Gondwana and opening of the Tasman Sea during the mid to Late Cretaceous (King & Thrasher, 1996; Strogen et al., 2017). After cessation of Late Cretaceous extension and associated thermal subsidence, contraction developed along the eastern margins of the basin from the Late Eocene to Early Oligocene, migrating westwards across much of the basin during the Late Miocene (King &

Thrasher, 1996; Stagpoole & Nicol, 2008; Reilly et al., 2015). Synchronous extension in north and contraction in the south of the basin developed in the Pliocene and continues to a lesser extent to the present day (King & Thrasher, 1996; Giba et al., 2010; Reilly et al., 2015). To the south of the basin, the oblique westward subduction of the Pacific plate beneath the Australian plate along the Hikurangi margin (48-41 mm/yr) transitions to continental collision and transpression along the Alpine Fault (35-30 mm/yr) (Beavan et al., 2002; Wallace et al., 2004).

The southern Taranaki Basin contains some of the most productive gas and oil fields in New Zealand (e.g., the Maari, Maui and Tui fields to the west; the Kapuni, Kauri, and Rimu fields to the northeast; and the Kupe Field to the east) (Fig. 2). Collectively, these fields contain most (~67%) of the estimated 1960 mmboe cumulative reserves from developing or producing fields in the Taranaki Basin (New Zealand Ministry of Business, Innovation and Employment, 2018). The southern Taranaki Basin comprises two structural domains; the Western Stable Platform (passive margin) and the Eastern Mobile Belt (active margin) (King & Thrasher, 1996). The Eastern Mobile Belt underwent contraction and structural inversion of Late Cretaceous normal faults mainly during the Late Miocene with subsequent extension and collapse of some inversion structures during the Pliocene (King & Thrasher, 1996; Nicol et al., 2005; Stagpoole & Nicol, 2008; Reilly et al., 2015). Structures within the Eastern Mobile Belt therefore include inversion and reverse faults and folds that provided closures for trapping petroleum, now the focus for active petroleum systems within the region (Fig. 2 and 3) (King & Thrasher, 1996; Reilly et al., 2015).

Recent studies and data compilation of *in-situ* stress within the Taranaki Basin have provided valuable information on near surface stress orientations (Rajabi et al., 2016) (Fig. 2), however, the magnitudes of stresses are still poorly constrained across the majority of the basin. Regional and limited local stress inversions of earthquake focal mechanisms indicate that the southern Taranaki Basin is located in the transition between normal/strike-slip/reverse regimes. In the North Island the maximum horizontal stress (S_{Hmax}) azimuth trends ENE-WSW (~075°) in a normal-strike slip regime

and in the South Island the S_{Hmax} azimuth trends ESE-WNW (~120°) within a reverse/strike-slip regime (Webb & Anderson, 1998; Sherburn & White, 2006; Townend et al., 2012). Extensive analysis of borehole stress-induced features yielded a mean ENE-WSW regional S_{Hmax} orientation (068°±22°) for the entire Taranaki Basin (Mildren et al., 2001; GMI, 2010; Rajabi et al., 2016, including references to Horan, 1997). This stress orientation is in agreement with the NW-SE extension suggested by the mapped normal faults, sub-parallel to the subduction trench to the east and the strike of the subducting slab beneath the basin (050°) (Giba et al., 2010; Seebeck et al., 2014b; Rajabi et al., 2016). Borehole studies indicated a normal to strike-slip regime north and immediately south-west of the Taranaki peninsula (Mildren et al., 2001; Mildren & Meyer, 2006; GMI, 2010). To date, the stress regime within the southern Taranaki Basin has not been established.

In this study, we focus on the central region of the southern Taranaki Basin containing hydrocarbon producing fields situated within the Western Stable Platform (Tui) and Eastern Mobile Belt (Maui, Maari-Manaia) structural domains (Fig. 3). The discovery of active petroleum systems in the region has resulted in numerous exploration and production boreholes along with the acquisition of numerous 3D seismic-reflection surveys, which together, enable the investigation of the effects of the present-day stress tensor on faults that may have influenced the migration and trapping of hydrocarbons. Previous interpretation of 2-D and 3-D seismic reflection surveys in the southern Taranaki Basin yielded fault strikes NNE-SSW to NE-SW with dip magnitudes ≥60° (Reilly et al., 2015; Fig. 2). With a mean ENE-WSW regional S_{Hmax} orientation sub-parallel to fault strikes and fault fault dip typically >60°, some of these faults are, in theory, favourably oriented for slip in a present-day strike-slip/normal stress regime (Fig. 1).

3. Determination of stress and fault structure

3.1. Stress orientation and magnitude estimations using borehole data

The shear and normal stresses on a fault are derived from the orientation of a fault plane with respect to the orientation and magnitude of the *in-situ* principal stress components (S_1, S_2 and S_3),

and with inclusion of the formation pressure (P_p), yield the effective principal stress components σ_1, σ_2 and σ_3 (Jaeger et al., 2009). Due to uncertainties associated with many of the parameters involved in the calculation of *in-situ* stress, the magnitude of maximum horizontal stress (S_{Hmax}) is typically difficult to quantify (e.g., Zoback et al., 2003).

Here, we assume that one of the principal stress components is vertical, which is consistent with earthquake focal mechanism (Sherburn & White, 2006) and stress inversions (Townend et al., 2012) from the region. The principal stress components can thus be written as S_v (vertical stress); S_{Hmax} (maximum horizontal stress); and S_{hmin} (minimum horizontal stress). The ratio S_{Hmax}:S_v represents the stress regime: S_{Hmax}:S_v <1 in normal stress regime; S_{Hmax}:S_v >1 for strike-slip regime; and S_{Hmax}:S_v~1 for a mixed normal/strike-slip regime (Fig. 1).

Formation (pore) pressure (P_p) is near hydrostatic in the southern Taranaki Basin, as documented in borehole drilling reports (based on mud weights; rare gas kicks; and cuttings shape not indicating caving; accessible through NZP&M (2018) and https://data.gns.cri.nz/pbe/); wireline formation tests summarised in Sykes, 2012); and consistent with the review of wireline formation tests across the Taranaki Basin (Webster et al., 2011). Leak-off tests measuring S_{hmin} magnitudes and formation integrity tests are reviewed in 47 boreholes located throughout the study area. S_v magnitude profiles are calculated for 11 boreholes: five in the Tui area (Amokura-1, Kahu-1, Matuku-1, Tui-1 and Tui SW-2); three in the Maari-Manaia region (Maari-1, Maari-2 and Whio-1); and three in the Maui area (Maui South-1, MB-P(8) and MB-Z(11)) (Fig. 3). S_{Hmax} azimuth and magnitudes are analysed in four of these boreholes: three in the Maari-Manaia region (Maari-1, Maari-2 and Whio-1), and one in the Tui region (Matuku-1) (Table 1; Fig. 3). Collectively these four boreholes cover a depth range of 750 to 4680 m (all reported depths are true vertical depth below sea level; TVDss; Table 1).

The orientation of S_{Hmax} and quality rankings are obtained from stress-induced features identified on borehole images, following the World Stress Map guidelines and criteria (Sperner et al., 2003; Zoback et al., 2003; Heidbach et al., 2016). In the four sub-vertical borehole sections analysed

(deviated <3°, and up to 13° for the uppermost imaged portion of borehole Whio-1), borehole breakouts and drilling-induced fractures form in the direction of S_{hmin} and S_{Hmax}, respectively. Unfortunately, image logs in boreholes MB-P(8), Maui South-1 and Tui-1 were not of sufficient quality to confidently interpret stress-induced features. These new data complement the S_{Hmax} azimuths derived from borehole images and earthquake focal mechanisms compiled by Rajabi et al. (2016).

The methods used to estimate stress magnitudes from borehole data in this work are detailed in Wiprut et al. (2000) and Zoback et al. (2003), and summarised herein. The overburden vertical stress S_v is calculated by integrating density logs in each borehole (Equation 1):

$$S_v = \rho_w g z_w + \int_0^z \rho(z - z_w) g \, dz \quad (1)$$

with z the depth in metres below sea level; z_w the depth of the seafloor below sea level; ρ_w the sea water density assumed to be 1050 kg/m^3; ρ the formation density; and g the acceleration of gravity.

To estimate the formation density in the upper section of boreholes typically lacking density logs, we use an average sediment compaction formula derived from Taranaki Basin boreholes (Equation 2; Athy, 1930; Armstrong et al., 1998) and a standard conversion from porosity (Φ) to density (Equation 3; Nafe & Drake, 1957):

$$\Phi\,(\mathrm{z}) = \Phi_0 \exp(-(z - z_w)/\mathrm{D}) \quad (2)$$

$$\rho = \Phi * (\rho_w - \rho_m) + \rho_m \quad (3)$$

where a surface porosity Φ_0 of 0.5 is assumed based on Armstrong et al. (1998); D is the exponential compaction coefficient adjusted from the value of 2265 m derived by Armstrong et al. (1998) to fit the density log in each borehole (see section 4.2); and ρ_m is the matrix density assumed to be 2650 kg/m^3.

S_{hmin} magnitudes are derived from 19 leak-off tests in 18 boreholes located throughout the southern Taranaki Basin, and 1 extended leak-off test (2 pressurisation cycles) in borehole Kahu-1, (Fig. 3; Research Data; for details on the interpretation of leak-off tests, see e.g. Zoback et al., 2003). For completeness, we also report results of 62 formation integrity tests in 37 boreholes. These tests are small-volume and low pumping rate injection tests performed on a short (~10 m) section of hole drilled ahead of a casing shoe after the casing was cemented. These measurements aim to test the integrity of the cementing and determine the pressure at which the injectivity of the formation begins to increase due to the opening of fractures. It is usually not known whether a natural or induced fracture opens—and thus whether the opening pressure is a direct measure of S_{hmin} magnitude. As pressure was measured at the surface rather than at the depth of the test, the weight of the drilling mud column is added to the pressure measured at surface. Pressure measurements are considered to be leak-off tests, and hence confident S_{hmin} estimations, if pressure and pumping data were available; and when a clear leak-off point was observed. For Kahu-1, the leak-off point reading was confirmed by the instantaneous shut-in pressure and formation propagation pressure. If the leak-off point was not reached, or if there was ambiguity in the interpretation of the pressure tests, the test was considered to be a formation integrity test. The latter tests are of low confidence and represent a potential lower bound to the S_{hmin} magnitude.

S_{Hmax} magnitudes are calculated using borehole breakout widths, indirect information on rock strength, and pressures while drilling, assuming a Mohr-Coulomb failure criterion (Equation 4; Barton & Zoback, 1988; Zoback et al., 2003).

$$S_{Hmax} = \frac{C_0 + 2\,P_p + \Delta P + \sigma^{\Delta T} - S_{hmin}(1 + 2\cos(2\theta))}{1 - 2\cos(2\theta)} \quad (4)$$

where $2\vartheta = \pi - \Phi$; Φ is the angle of borehole breakout ("breakout width") in radians; C_0 the unconfined compressive strength (UCS); ΔP the pressure difference between the formation and the borehole; and $\sigma^{\Delta T}$ the thermal stress effect (negligible in the southern Taranaki Basin based on recorded temperature logs).

The UCS at the breakout depth is estimated from acoustic compressional wave slowness (Δtc) logs (also called sonic logs). Several empirical relationships between Δtc and UCS have been developed and calibrated to laboratory strength tests on samples of various lithology (see review by Chang et al., 2006). However, laboratory strength tests are rarely conducted in the Taranaki Basin, and lithologies are typically mixtures of sandstones, siltstones and mudstones, so we adopt a cautious two-step approach to estimating UCS rock strength. (1) We assign a preferred empirical equation based on the dominant lithology (sandstone or mudstone) to select the most likely representative UCS (and hence S_{Hmax} magnitude; Table 2). (2) We also provide a range of UCS values (represented as error bars on the S_{Hmax} magnitudes) using the empirical equations developed for sandstones and shales (Table 2). In boreholes Maari-1 and Maari-2, mudstones are defined as having gamma-ray log values >80 API, and sandstones <80 API, based on cuttings descriptions reported by Halliburton Australia Pty Ltd (1999) and OMV New Zealand Limited (2003). For borehole Whio-1, intervals of dominant lithologies were selected based on detailed descriptions of cuttings (Wyman & Smith, 2015).

Finally, to provide bounds for the minimum value of S_{hmin} in a normal stress regime, and the maximum value of S_{Hmax} in a reverse stress regime, we assume that the formation is critically stressed (Barton et al., 1995), for which Jaeger et al. (2009) showed (Equation 7):

$$\frac{S_1 - P_p}{S_3 - P_p} = \left[(\mu^2 + 1)^{1/2} + \mu\right]^2 \qquad (7)$$

where μ is the coefficient of friction estimated at 0.7 (Byerlee, 1978; GMI, 2010). In a normal stress regime, $S_1=S_v$ and $S_3=S_{hmin}$; and in a reverse faulting regime, $S_1=S_{Hmax}$ and $S_3=S_v$.

3.2 Evaluation of uncertainties in S_{Hmax} magnitude calculations

S_{Hmax} magnitude is typically the most difficult parameters to constrain from borehole data, and estimating S_{Hmax} magnitudes from borehole breakout width and rock strength has caveats, including the assumption of a failure criterion is valid; that the borehole is perfectly circular; and that the rock

strength is known at the breakout location (e.g. Zoback, 2007; Valley and Evans, 2019). However, with only one focal mechanism available in the study area, constraints on S_{Hmax} magnitudes from borehole data are valuable and have the benefit of informing on stresses and their variations in the shallow crust.

The first source of uncertainty is the breakout width measurement in borehole Whio-1 because one of the breakout edges often lies in-between the resistivity imager pads (such as in Fig. 4), and only those breakouts where both sides were observed were kept for S_{Hmax} magnitude estimations.

The main uncertainty on S_{Hmax} magnitude is the rock strength at the borehole depth at which breakouts form. The empirical equations used here to convert acoustic compressional wave slowness from downhole measurements into UCS were developed mostly in the Gulf of Mexico and North Sea, where sandstones and mudstones are well differentiated, and calibrated by laboratory rock property testing (Chang et al., 2006, and references therein). In the southern Taranaki Basin, lithologies are commonly muddy sandstones and sandy mudstone and can be interlayered, which limits the applicability of these equations. Using a range of UCS derived from equations based on sandstones and mudstones permits an estimate of the possible S_{Hmax} magnitude range (Fig. A.2).

It is also questionable if the acoustic compressional wave borehole measurements are sufficiently characteristic of the rock strength in the southern Taranaki Basin, and of high enough depth resolution to identify thin units of varying rock strength. As presented in Fig. 4, breakouts can be confined to moderately cemented carbonate units, which might have different UCS to their surrounding lithologies (even though the acoustic compressional wave log doesn't show variation between the partly cemented units and their surrounding lithologies). The location of borehole breakouts within partially cemented units indicates that these lithologies are more prone to fracturing, which may affect fluid migration and seal capacity at metre-scales. It is worth noting that, although the neutron porosity log shows a high value at the base of the partially cemented area (Fig.

4), it is within the variations observed above and below this interval, and would thus not provide a characteristic UCS estimation.

Despite these limitations on UCS estimations, the range and variability of UCS values derived from acoustic compressional wave slowness logs in the studied boreholes (Appendix 1) are consistent with laboratory tests conducted on cores recovered between 3529 and 3629 m depth in boreholes Pohokura-1 and Pohokura-2 north of the Taranaki Peninsula (Shell Todd Oil Services Limited, 2002) which contain similar lithologies to those in southern Taranaki Basin boreholes. In the two Pohokura boreholes, the UCS of fine to coarse grained sandstone with intercalated mudstone beds measured in laboratory ranges between 17 and 56 MPa for samples of 7.7 to 13% porosity (n=18 samples; no correlation between porosity and UCS). Two additional low-porosity samples yielded UCD of 88 MPa (5.2% porosity) an 92 MPa (2.3% porosity). This study mentions that values measured during laboratory tests are in general lower than those measured under confining stress, as would be the case in a borehole. These few laboratory values are consistent with those derived from boreholes data (Fig. A.2) so we are therefore confident that the S_{Hmax} estimations are reasonable.

Reducing uncertainties on estimates of S_{Hmax} magnitude would be best achieved by conducting mechanical rock property testing, on samples with a range of natural gamma-ray, density and resistivity downhole measurements. Based on experience from other sedimentary basins such rock property studies could reduce uncertainties on UCS and S_{Hmax} magnitude by as much as a factor of two (e.g., Chang et al., 2006).

3.3. Structural model

To understand the potential influence of the present-day stress field on the up-fault migration of hydrocarbons we utilise the geometry of faults mapped in 3D seismic reflection volumes (Thrasher et al., 2018). Faults and time equivalent horizons used in this study have been mapped over a region of 5250 km^2 within the study area from an amplitude balanced post-stack merge of open-file 3D seismic reflection survey (PGS Taranaki Megasurvey, which includes the Maui-3D, Kokako-3D, Tui-3D

and Opunake-3D), complemented with the recent open-file releases of Maari-3D, Tui-Ext-3D and Matuku-3D. In addition, we used the closed-file Kaka-3D seismic reflection surveys (courtesy of OMV New Zealand Ltd.). A total of twenty time-equivalent horizons comprising the entire Late Cretaceous to Recent sedimentary sequence (constrained by biostratigraphy in 26 boreholes across the study area; Roncaglia et al., 2013) were interpreted on a uniform interpretation seed line grid (1250 x 1250 m) oriented approximately perpendicular and parallel to the predominant structural trends (Thrasher et al., 2018) using Paradigm ® SeisEarth. Near surface horizon (<300 ms TWT below the seafloor) ages are poorly constrained and estimated to be ≤1.5 Myr old. Horizons relevant to this study, such as the base Pliocene unconformity in the Maari-3D, were autopicked to produce an accurate surface interpretation at the resolution of the seismic data (12.5 x 25 m Inline/Xline spacing). Faults identified in seismic amplitude and coherency attributes were mapped at varying resolutions (typically 625 m along strike) within the horizon interpretation seed grid set to a maximum of 5 seconds two-way travel time (TWT) (example of fault trends at base Oligocene shown in Fig. 3). Due to small displacements and the sub-vertical nature of the faults in proximity to the Maari, Moki and Manaia boreholes (including Whio-1), faults were mapped with a line spacing of ~125 m along strike. Three-dimensional triangulated fault surfaces were then modelled in TWT and depth converted using SKUA-GOCAD ™. Time-depth conversion utilised velocity data from 26 boreholes within the study area to generate a 3D interval velocity volume using the mapped horizons in a layer cake approach (Viskovic et al., 2019). On average, the model depth error at basement was generally <1% at depths between 3400 and 4200 m. Faults determined to be active in the present day are characterised by seafloor scarps (e.g., Cape Egmont Fault; Nodder, 1993) and/or by seismic reflectors displaced at or immediately below seafloor. Faults considered inactive within the last ~1 Myr have no detectable normal displacement within 100 ms TWT of the seafloor. In practice, these faults may have been recently active but have sub-resolution displacement to the seafloor.

3.4. Slip tendency estimates

The orientations and magnitudes of the principal stresses relative to pre-existing faults, together with fault and host rock properties, control the ability of faults to slip and generate earthquakes (Morris et al., 1996; Zoback, 2007 and references therein; Alt & Zoback, 2017). Slip on a fault may also lead to rupture of hydraulic seals within fault zones, producing transient or permanent increases in fracture permeability (Sibson, 1994; Barton et al., 1995), which have the potential to produce leakage from petroleum reservoirs (Rinaldi et al., 2014). Slip tendency, defined as the ratio of shear (τ) to effective normal stress (σ_n) ($T_s = \tau / \sigma_n$), quantifies how close to failure a fault of a defined orientation is within a given stress field. In an Andersonian faulting regime, faults striking parallel to the maximum horizontal stress (S_{Hmax}) azimuth and dipping 60° are best oriented for slip in a normal stress regime, whereas sub-vertical faults striking 30° either side of S_{Hmax} azimuth are best oriented for slip in a strike-slip stress regime (Fig. 1; Anderson, 1905). If the two highest principal stress components are S_v and S_{Hmax} and are of similar magnitude, both normal and strike-slip faults have high slip tendency (Fig. 1b).

We map the fault slip tendency using Move™ software. The mapping of slip tendency values onto stereonets shows the slip tendency for all possible poles to faults. Faults are triangulated to accommodate their non-planarity. Each pole to plane on the stereonet correspond to one of these triangles, i.e. a small portion of the fault surface. We also show 3D views of slip tendency mapped onto the Cape Egmont Fault and two representative minor faults (striking NE-SW and E-W) within the Maari-Manaia field area (See Fig. 3 and 6, respectively). The Cape Egmont Fault is the largest normal fault in the southern Taranaki Basin, with a Plio-Pleistocene vertical displacement of up to ~2500 m, dominated by normal displacement and possibly a small amount of right-lateral slip (Nicol et al., 2005; Reilly et al., 2015). The Cape Egmont Fault is a Late Cretaceous normal fault, having experienced positive inversion in the Late Miocene and negative inversion/extensional collapse in the Pliocene-Recent (King & Thrasher, 1996; Reilly et al., 2015). As a result, this major fault has

variable strike and dip orientations, laterally and with depth (Fig. 2 and 3), thus capturing many of the fault orientations observed elsewhere within the southern Taranaki Basin.

4. Stress magnitudes, 3-D fault map and slip tendency

4.1. S_{Hmax} azimuth: dominantly ENE-WSW, with localised rotations

The new S_{Hmax} azimuths derived from stress-induced features in boreholes (mainly borehole breakouts with rare drilling-induced tensile fractures) predominantly trend ENE-WSW: 071°±10° (1σ error; Heidbach et al., 2016) in borehole Whio-1; and 076°±6° in borehole Matuku-1 (Table 1; Fig. 5 and 6). Altogether, stress-induced features in these three boreholes span between 1210 and 4680 m depth (Table 1; Fig. 5). Dipole sonic log interpretation in borehole Whio-1 also indicates an 070° S_{Hmax} azimuth (Wyman & Smith, 2015). These orientations are similar to the regional 068°±16° (A-B quality, in 39 boreholes) S_{Hmax} previously reported by Rajabi et al. (2016) for the Taranaki Basin.

The azimuth of S_{Hmax} locally departs from the regional orientation. The Maari-1 and Maari-2 boreholes located between 760 and 2160 m, show a NE-SW S_{Hmax} azimuth (030°±8° and 039°±9°, respectively; Table 1), which is different from nearby Whio-1 borehole. The upper and lower part of Maari-1 also show slightly different mean S_{Hmax} azimuth (24°±7° and 34°±5°, respectively). In the Whio-1 borehole, S_{Hmax} azimuth rotates gradually by up to 30° about the mean over 150 m-long depth intervals. Rotations are clockwise between 1217 and 1316 m, and then counter-clockwise to 1350 m; and again between 1800 and 1950 m (Fig. 7a). The S_{Hmax} azimuth rotation between 1200 and 1350 m in Whio-1 is defined by eight borehole breakouts (with uncertainty of ±10° due to the breakout edges being located between the imaging tool pads; Fig. 4 and 7), and confirmed by the borehole ellipticity measured by 4-arm caliper measurements. The borehole elongation direction does not coincide with the low-side azimuth of the borehole and is thus interpreted as being caused by *in-situ* stress rather than drilling (borehole deviation ≤13°; Heidbach et al., 2016).

The S_{Hmax} rotation between 1200 and 1350 m in Whio-1 is attributed to the perturbations caused by a fault mapped on seismic-reflection lines and its damage zone, which likely intersects the borehole at ~1300 m. Indeed, a seismic-scale fault intersect Whio-1 borehole at ~ 1350 m (uncertainty on seismic resolution bounds the fault/borehole intersection between 1260 and 1470 m; Fig. 7b). The switch of S_{Hmax} azimuth rotation direction at ~1316 m in the Whio-1 well coincides with two faults observed on the image log, striking 074° at 1300 m, and 101° at 1306 m, both dipping 73° southwards (Fig. 7a, c). Sedimentological analysis of the image log by Wyman & Smith (2015) shows a change of bedding plane dip directions at 1300 m (SSE above 1300 m and ENE below) interpreted as caused by a fault. Unfortunately, it is not possible to measure the direction, magnitude or sense of displacement of these faults on the image log and we were unable to determine if they were predominantly normal or strike-slip. The seismic-scale fault has a similar strike (mean of 099°, mean dip of 75°) to the fault identified on the image log at 1306 m, and to the fractures identified in the entire borehole image log (mean fracture strike 095°, with various dip magnitudes ranging from 28° to 84° and a mean of 58°; n=17 fractures). Based on seismic reflection data the upper tip of this fault lies at ~200 ms TWT (150 m) below the seafloor (Fig. 7b) with a maximum vertical offset of 10-15 m on the base Pliocene unconformity. In map view, Late Miocene channels intersected by the fault at high angles show no demonstrable horizontal offset at the resolution of the 3D seismic data and therefore this fault is considered to be predominantly normal dip-slip. The rotation of the S_{Hmax} azimuth between 1800 and 1950 m cannot be attributed to a specific fault at borehole or seismic scales. This rotation may thus be related to a fault located near Whio-1 rather than intersecting it, and of too small dimensions and displacement to be identified in the 3D seismic reflection data.

Local S_{Hmax} azimuth rotations have been noted in the Taranaki Basin (Rajabi et al., 2016) and documented worldwide (e.g., Yale, 2003; Barton & Zoback, 1994; Tingay et al., 2010; McNamara et al., 2015; Rajabi et al., 2017a; Heidback et al., 2018), but these rotations have not been considered to date in stress studies of the southern Taranaki Basin. As the slip tendency of faults depends on the stress orientation and magnitudes relative to the fault orientation, local variations of stress

orientations and magnitudes as well as variations of fault geometry affect the slip tendency of faults in the southern Taranaki Basin (see section 4.3 for further discussion).

4.2. Fault map

Fault mapping confirms previous interpretations of the general NE-SW trend of fault systems in the study area (e.g., King & Thrasher, 1996; Reilly et al., 2015), with higher resolution. In the Maari-Manaia region, numerous low-displacement faults cross cut the inversion anticlines striking E-W (085°– 100°); ENE-WSW (055 – 065°); and NE-SW (035° – 045°), by decreasing order of cumulative length, have been recently identified (cf. Wunderlich & Mayer, 2018) and mapped in this study (Fig. 3, 6). These minor faults, one of which intersects the Whio-1 borehole (see Sections 4.3 and 5.2), may significantly influence both the lateral and vertical migration of hydrocarbons.

4.3. Stress magnitudes: a strike-slip to normal stress regime

Borehole data analysed in this study show a strike-slip to normal stress regime in the central part of the southern Taranaki Basin. The S_v magnitude gradient is 20.7±1.6 MPa/km at 2000 m (n=9 boreholes across the study area; error is 2σ; Fig. 8a and A.1). The S_v magnitude gradient increases slowly with depth as rock density increases with depth under compaction (Fig. 8a and A.1; 18.9±1.4 MPa/km at 1000 m (n=10); and 21.5±0.6 MPa/km at 3000 m (n=6)). The greatest lateral variations of rock density are observed at depths shallower than 2.1 km (density ~0.2 g/cm^3 higher in the Maari area than in the Maui area; Fig. A.1). At these shallower depths we used variable compaction coefficients (800 to 2265 m^{-1}) to estimate rock density where downhole logs were not acquired. These density variations have limited effect on the S_v gradients (<1 MPa/km) compared to other parameters associated with stress magnitude calculations.

Leak-off tests show a range of S_{hmin} magnitude across the southern Taranaki Basin, with fracture gradients (S_{hmin} magnitude divided by depth) ranging between 12.5 and 18.6 MPa/km, with a mean of ~17.6 MPa/km (Fig. 8b-c; ratio of mean S_{hmin}:S_v of about 0.85). Most of the leak-off tests were

undertaken at <1600 m, but the three deeper leak-off tests are consistent with the shallower measurements. The lowest fracture gradient derived from leak-off tests corresponds with the lower bound of S_{hmin} for normal faults at frictional failure (Eq. 7; ~13 MPa/km, varying slightly depending on the borehole and depth, hence S_v magnitude). Low confidence lower bounds of S_{hmin} magnitude obtained from formation integrity tests are generally lower than S_{hmin} estimates from leak-off tests. The spread in S_{hmin} magnitudes from leak-off tests is attributed to the condition in which each test was performed: depth, lithology (which varies from mudstone to sandstone), and borehole shape just below casing.

S_{Hmax} magnitudes in the Maari-1 and Whio-1 boreholes are slightly higher or lower than S_v, indicating a strike-slip to normal regime ($S_{hmin}<S_v\leq\approx S_{Hmax}$ to $S_{hmin}<S_{Hmax}\leq\approx S_v$, respectively), with S_{Hmax}:S_v ratios of 0.8 to 2.3 for Maari-1, and 0.9 to 1.6 for Whio-1, both boreholes having a median ratio of 1.1 (Fig. 8c). The deeper part of Maari-2, drilled at the same depth (1340-1455 m) and geological formation (Moki Formation) as Maari-1, has similar S_{Hmax}:S_v ratios to those in Maari-1 (0.9 to 1.3, median of 1.2). The error bars on S_{Hmax} magnitudes reflect the variability in UCS assuming either sandstone (lower bound) or mudstone (higher bound) lithologies. A wide breakout (101°) in Maari-1 yielded an S_{Hmax} magnitude higher than the theoretical limit at frictional failure for reverse faults, and we follow Valley and Evans (2019) in using only borehole breakouts with width <90°.

The shallow interval of Maari-2 (965 – 1250 m) shows higher S_{Hmax} magnitudes (S_{Hmax}:S_v ratio of 1.2 to 2.7, median of 1.5) than in the deeper section (Fig. 8c). This higher S_{Hmax} magnitude is linked to the low acoustic compressional wave slowness (< 80 µs/ft) between 951 and 1228 m, yielding a high UCS (ranging between 40 and 100 MPa) (Fig. A.2). This interval comprises lithologies varying from sandstone to mudstone (Upper and Mid-Manganui Formation, including the Sw and M2A sands; OMV New Zealand Limited (2003)). By contrast, the underlying borehole section intersecting similar lithologies (though overall more sandy; Mid Manganui and Moki Formations, OMV New Zealand Limited (2003)), has a compressional wave slowness of ~90 µs/ft and UCS< 50 MPa (Fig. A.2).

Laboratory testing of rock samples are needed to clarify what controls the acoustic velocity in these lithologies in the southern Taranaki Basin, how it affects the rock strength estimations, and possible effects on stress magnitudes.

In contrast to the boreholes in the Maari-Manaia area, the Matuku-1 borehole shows a dominantly normal faulting regime, with S_{Hmax}:S_v ratio of 0.7 to 1.1, median of 0.9, consistent with active normal displacement on the active Cape Egmont Fault ~30 km to the east (Nodder, 1993) (see Fig. 3 for location). The difference in stress regime between the Matuku-1 borehole, and those of the Maari-Manaia region may be due either to its different depth or location within the southern Taranaki Basin. Indeed, the Matuku-1 image log samples deeper (3900-4675 m) intervals than the Maari-1, Maari-2 and Whio-1 boreholes (765-2630 m), and is located on the Western Stable Platform that has remained undeformed during the Neogene (Fig. 2). This location contrasts with wells situated within the Eastern Mobile Belt and is discussed further in Section 5.2.

4.4. Fault slip-tendency analysis

The mapping of slip tendency in 3-D over the surfaces of the three faults presented in Fig. 9 is representative of the possible slip tendencies on faults active in the last 1 Myr in the southern Taranaki Basin. The pole to planes on the stereonets represent small patches of each of the three triangulated fault surfaces. Given the local variability in S_{hmin} magnitude and S_{Hmax} azimuth, and uncertainties in S_{Hmax} magnitudes, we consider four scenarios compatible with borehole data to estimate the slip tendency (T_s) of the three faults in Fig. 9. For each of the three faults S_v is fixed at 20.7 MPa/km, representative of a depth of 2 km. Three of the four scenarios assume an S_{Hmax} azimuth of 070°: a normal faulting regime as measured in Matuku-1 (S_{Hmax}:S_v=0.9; Fig. 9a); a strike-slip regime as measured in Whio-1, Maari-1 and the bottom section of Maari-2 (S_{Hmax}:S_v=1.1; Fig. 9b); and a strike-slip regime as measured in the upper section of Maari-2 (S_{Hmax}:S_v=1.5; Fig. 9d). The fourth scenario assumes an S_{Hmax} azimuth of 050° and a strike-slip regime with S_{Hmax}:S_v=1.1 (Fig. 9c),

which represents zones of S_{Hmax} azimuth rotations from the regional trend such as those observed in the Maari-1, Maari-2 and Whio-1 boreholes.

In the three stress scenarios with S_{Hmax}:S_v =0.9 or 1.1, none of the representative faults are in conditions of failure. This is demonstrated by the Mohr circles not touching the Mohr-Coulomb failure envelope for cohesionless faults with a friction coefficient of 0.6, a lower bound of typical values (Byerlee, 1978) (Fig. 9a-c). As expected by failure theory in strike-slip regimes, the maximum value of slip tendency increases as the S_{Hmax}:S_v ratio increases (appearing as a larger Mohr circle, Fig. 9d). The maximum slip tendencies observed are: 0.2 for the normal faulting regime with S_{Hmax}:S_v=0.9; 0.3 for the strike-slip regime with S_{Hmax}:S_v=1.1; and 0.6 for the strike-slip regime with S_{Hmax}:S_v=1.5. It is only in this latter case that very small regions of the three faults best oriented for slip along the geometrically variable fault surfaces have a slip tendency nearly high enough for slip with a friction coefficient of 0.6 (1% of fault surfaces with $T_s \geq 0.58$; an additional 7% of fault surfaces with 0.55<Ts<0.58) (Fig. 9d).

The non-planar 3D geometry of faults has a large effect on their tendency to slip. In each case, the slip tendency increases as the local fault geometry approaches a pure Andersonian faulting configuration, i.e. dipping 60° and striking parallel to S_{Hmax} for a normal stress regime; and sub-vertical and striking 30° either side of S_{Hmax} (i.e., striking either 40° or 100°) for the strike-slip stress regime (e.g., Fig. 1). The faults in the Maari-Manaia region are thus optimally oriented for slip in a strike-slip/normal regime with a 070° S_{Hmax} azimuth. The effect of non-planar fault geometry is particularly clear for the Cape Egmont Fault, which has along-strike corrugations that produce varying slip tendency. An S_{Hmax} azimuth to 050° in a strike-slip regime (Fig. 9c) forms vertical "corridors" of higher slip tendency on the Cape Egmont Fault (but insufficient for slip), due to the alternation of areas striking either NNE-SSW (000° – 030°) or ENE-WSW (064° – 080°) having higher slip tendency than those striking NE-SW (030° – 064°).

5. Discussion

5.1. Regional fault orientation and stress from borehole data

The new borehole data indicate a strike-slip/normal stress regime in the Maari-Manaia area, and normal faulting regime further west in the Tui region (borehole Matuku-1). The dominant ENE-WSW S_{Hmax} azimuth is consistent with previous borehole data sampled from depths <4 km (Rajabi et al., 2016 and references therein). Focal mechanisms at 7-35 km depth in the Cape Egmont Fault Zone in the northern part of the studied area are strike-slip (Sherburn & White, 2006), and the 1974 Mw 5.5 Opunake earthquake was identified as oblique normal (Webb & Anderson, 1998; Fig. 2) with fault planes generally parallel and perpendicular to the dominant fault trends in the region (e.g., Fig. 2). The stress magnitudes estimated from borehole data in this study are consistent with a strike-slip stress regime identified from borehole studies north of the study area in hydrostatically pressured zones (Te Kiri prospect; GMI, 2010: Pohokura and Moana prospects; Mildren et al., 2001; Mildren & Meyer, 2006).

Although the normal stress regime recorded in the Matuku-1 borehole is based on data deeper than the strike-slip/normal stress regime in boreholes of the Maari-Manaia area, we suggest that the change of stress regime reflects the southward transition from extension to contraction associated with the change from oblique subduction along the Hikurangi margin to transpression along the Alpine Fault (e.g., King & Thrasher, 1996, Wallace et al., 2004; Giba et al., 2010; Townend et al., 2012; Reilly et al., 2015). The normal stress regime in Matuku-1 is thus consistent with its location in the Western Stable Platform further away from the transition from extension to contraction than the Maari-Manaia area. The strike-slip/normal stress regime in the Maari-Manaia area is also consistent with its location to the north of this transition which occurs towards the southernmost margin of the Taranaki Basin.

5.2. Borehole-scale S_{Hmax} azimuth rotations near faults

Local rotation of S_{Hmax} azimuths from regional trends are commonly attributed to the influence of nearby active faults (e.g., Barton & Zoback, 1994, Yale, 2003; Hickman & Zoback, 2004; Tingay et al., 2010; Davatzes & Hickman, 2010; McNamara et al., 2015), but also to variations in mechanical properties of faulted strata (Heap et al., 2010; Rajabi et al., 2017a and references therein; Fig. 1d) or fluid pressure (Rice, 1992). Evaluating these local variations is needed for reservoir development and earthquake hazard assessment (Rajabi et al., 2017b).

The 30° anticlockwise difference of Maari-1 and Maari-2 boreholes (030° and 039°) from the regional S_{Hmax} trend (~070°) is consistent with the trend of underlying faults. The S_{Hmax} azimuth in these boreholes is parallel to nearby minor normal faults (Fig. 6) and to the Maari Fault, a Late Miocene inversion fault with ≥1 km of vertical separation on the base Oligocene horizon (see Fig. 3 and 6 for location).

The seismic- and borehole-scale faults identified in the zone of ~30° clockwise S_{Hmax} rotation in Whio-1 are favourably oriented for slip in the stress regime determined for the Maari-Manaia region (strike-slip/normal with S_{Hmax} azimuth ~070°). The seismic fault sub-vertical and striking 099° is favourably oriented for slip under a strike-slip regime. The ENE-WSW (074°) and ESE-WNW (101°) strikes of the two image log scale faults suggest that these different orientations are most likely to be normal and strike-slip, respectively (Fig. 1b). The dip magnitude of these faults (73°) is intermediate between a pure Andersonian normal (dip magnitude of 60°) and strike-slip (dip magnitude of 90°) faulting (Fig. 1). This orientation is similar to that of other normal faults mapped in the southern Taranaki Basin (Reilly et al., 2015), which are thus favourably oriented for slip.

The seismic-scale fault with S_{Hmax} rotation intersecting the Whio-1 borehole has likely been inactive for at least ~1 Myr because it does not appear to displace younger seismic reflectors (Fig. 7b). This S_{Hmax} rotation near the inactive fault could arise due to variations in the strength of rock across the fault and/or because the differences between horizontal stress magnitudes are small (Rice, 1992;

Yale, 2003; Hickman & Zoback, 2004; Ferrill et al., 2017; Boulton et al., 2017). Alternatively, it is possible that this favourably oriented fault and similarly nearby faults are presently active with sub-resolution displacements near the seabed, or that they are active but remain blind (i.e. do not offset the seafloor).

Whether faults are recent and formed in the contemporary stress regime, or inactive, the seismic-scale fault zone intersecting the Whio-1 borehole likely contains a combination of faults and fractures striking 070° and 100°, which are favourably oriented for reactivation in the current stress regime. The stress magnitudes and frictional properties of these small-scale faults are inferred to control their reactivation potential, although have not been explicitly studied here. Irrespective of why the stress rotations occur, it is clear that the S_{Hmax} azimuth can change by tens of degrees over length scales of ~100 m or less (both laterally and vertically), and these changes affect the potential for fault slip locally.

5.3. Fault slip and potential associated increases in permeability

The slip tendency models show that, assuming that faults are cohesionless with a coefficient of friction of ~0.6, the stress magnitudes are not sufficient to reactivate faults and increase their potential to act as fluid conduits (e.g., Barton et al., 1995; Townend & Zoback, 2000) even if faults are favourably oriented for slip (Fig. 9). Based on the observed variations in the S_{Hmax} azimuth and magnitude observed in the boreholes each of the four stress scenarios considered may apply to sections of faults and their damage zones. As predicted by frictional theory, the transition from a normal to a strike-slip regime increases the overall slip tendency of faults. Slip on cohesionless faults and fractures would only be initiated with a high S_{Hmax}:S_v ratio (≥1.5). Such a high stress magnitude ratio was only observed in the upper section of the Maari-2 borehole. These observations are supported by faults mapped in the Maari-Manaia region being favourably oriented to undergo normal (ENE-WSW) and strike-slip (NE-SW and E-W) faulting in the present stress regime (Fig. 6c), but show no contemporary displacement resolvable on the seismic reflection data. By contrast, to

the north of the study area, the active seafloor fault trace of the Cape Egmont Fault (Nodder, 1993; Nicol et al., 2005), active fault traces on the Taranaki Peninsula (Townsend et al., 2008, 2010; Mouslopoulou et al., 2012) and crustal seismicity (Webb & Anderson, 1998; Sherburn & White, 2006; Townend et al., 2012) indicate that normal faults are at, or close to, failure.

Several other factors could facilitate fault slip on pre-existing faults within the southern Taranaki Basin in the contemporary stress regime. The mechanical properties of fault zones and their associated rock properties, such as fault gouge having low coefficients of friction with respect to the host rock (e.g., Boulton et al., 2017; Ferrill et al., 2017), may facilitate slip at lower stress ratios. Increases in pore pressure, as documented in the Taranaki Basin outside of the study area (Webster et al., 2011), would increase slip tendency by decreasing the effective normal stress. Such increases in pore pressure may also be associated with modifications of the entire stress regime, as documented in the northern Taranaki Basin (Mildren et al., 2001; Mildren & Meyer, 2006). Fault zones may also have different elastic properties and pore pressure conditions compared to its surrounding rocks, which could also facilitate mis-oriented parts of mature faults to slip, as suggested by Rice (1992) for the San Andreas Fault, and Sherburn & White (2006) for the western Taranaki region. Depending on the frictional and elastic characteristics of the faults in the southern Taranaki Basin, it is thus possible that some areas of faults are able to slip in the current stress regime. In addition, it is likely that all four stress scenarios based on borehole data presented here apply to various faults at once, and even to different parts of each fault surface. A probabilistic assessment of potential fault slip in the study area (e.g., Walsh III & Zoback, 2016) is thus recommended to include natural geological variabilities described herein in earthquake risk assessment.

High dilation tendency, defined as the normal to differential stress ratio ($T_d = (\sigma_1 - \sigma_n)/ (\sigma_1 / \sigma_3)$), and the combined effects of high slip and dilation tendencies ($T_{sd} = T_s + T_d$) have also been correlated to enhanced fault permeability (Gudmundsson et al., 2002; Ferrill & Morris, 2003; Jolie et al., 2016).

Establishing correlations between these stress parameters and enhanced fault permeability also depends upon a number of factors, including: (1) the detection of contemporary permeability zones, (2) the limitations of using a uniform stress field orientation and magnitude, and (3) additional geological factors that may limit fracture connectivity at reservoir scale (Jolie et al., 2016). Slip and dilation tendency analysis in the Kupe area of the southern Taranaki Basin, east of the study area, has previously suggested that faults parallel to S_{Hmax} are critically stressed and therefore most likely to accommodate up-fault fluid migration (Hemming-Sykes, 2012). However, when compared to the locations of inferred gas chimneys on faults these predictions are no better than predictions assuming that high permeability zones are randomly distributed over the fault surface (Hemming-Sykes, 2012). These observations suggest that, for the southern Taranaki Basin, slip and dilation tendency estimations using regional stress and fault-geometry may be of limited predictive value for fault permeability. The apparent predictive limitations of the geomechanical techniques could, if correct, reflect a number of factors, either not captured by the technique and/or not recorded by the available data. This paper highlights short wavelength (≤100 m) variations in stress orientations and magnitudes, which could not be incorporated into the study of Hemming-Sykes (2012), and were not accounted for in the fault permeability predictions. We believe that local variation in stresses coupled with local variations in mechanical properties of the rocks (e.g., Ferrill et al., 2017) and of orientations of the faults could have a profound effect on structural permeability. Therefore, we concur with previous workers (e.g., Hemming-Sykes, 2012; Ilg et al., 2012; Jolie et al., 2016; Nicol et al., 2017) in suggesting that even if the theory underpinning the models is correct, a great understanding of stress conditions and fault geometries at a local scale is required to realise the full potential of geomechanical techniques for prediction of fault permeability.

6. Conclusion

The southern Taranaki Basin is an example of basin with several successive phases of extension and contraction with numerous faults, where extensive petroleum borehole and seismic reflection

datasets allow us to test the potential for faults to slip and conduct fluid flow in the current stress regime. Analysis of borehole images and wireline logs from four boreholes, and compilation of leak-off tests throughout the study area, indicate a contemporary strike-slip/normal stress regime with ENE-WSW S_{Hmax} azimuth, consistent with previous studies. Local variations up to 30° in the orientation of S_{Hmax} from the regional trend are most likely related to pre-existing subsurface structures. Variations in the orientation of S_{Hmax} of a similar magnitude with depth are also documented in the Whio-1 borehole and coincide with the intersection of a low displacement (10-15 m) normal fault mapped on 3D seismic reflection data. Fault orientations observed at borehole and seismic scales in the Maari-Manaia region are favourably oriented for slip in the current stress regime, however, slip activity on these local faults appears to have ceased at least 1 Myr ago. The local rotation of S_{Hmax} azimuth within Whio-1 borehole may therefore be related to either displacement on the fault plane or fractures of the damage zone below the resolution of the seismic data; or by the different frictional or elastic properties within the fault zone. Stress scenarios based on the data from this study are used to examine slip tendency on representative faults. Slip tendency analysis indicates that both Pliocene and active faults are favourably oriented for slip in either normal (ENE-WSW-striking faults), strike-slip (NE-SW and E-W-striking faults) or strike-slip/normal stress regimes, but are not at present critically stressed (i.e., Ts >0.6) assuming a Mohr-Coulomb failure criterion with coefficients of friction of 0.6. Faults may be closer to failure through increases in pore pressure, increases in the magnitude of S_{Hmax}, and/or by a lower coefficient of friction within fault zones. These observations, combined with local stress orientation variability over scales of $10^2 – 10^4$ m and limitations of available data for quantifying stress magnitudes in the southern Taranaki Basin, make stress-based predictions of enhanced fault permeability of uncertain value without consideration of a range of geologic factors that contribute to subsurface fluid flow.

Acknowledgements

This project is funded by the Ministry of Business, Innovation and Employment through the GNS Science-led research programme on New Zealand petroleum source rocks, fluids, and plumbing

systems (contract C05X1507). We thank OMV New Zealand Ltd. for the use of the Kaka 3D seismic reflection survey and for providing and allowing publication of Matuku-1 and Whio-1 borehole data; and Petroleum Geo-Services for access to the Taranaki MegaSurvey. The Mohr circles were plotted using MohrPlotter software developed by Richard W. Allmendinger. We thank Paradigm for the academic license of SeisEarth® and SKUA-GOCAD™ used for seismic interpretation, depth conversion and three-dimensional modelling. Karsten Kroger, Richard Sykes and Rob Funnell are thanked for their reviews of an early version of this manuscript, and Dr. Rajabi for discussions on Maari-1 image log. Finally, we thank Dr. Gamboa and an anonymous reviewer for useful comments on this manuscript, as well as Dr. Alves for editorial handling and comments.

Appendix

Figure A.1: Estimation of S_v magnitude.

Figure A.2: Estimation of S_{Hmax} magnitude for the four study wells.

Research Data Related to this manuscript

Table of formation integrity test and leak-off test data. Massiot, C., 2019. Data for: Effects of regional and local stress variabilities on fault slip tendency in the southern Taranaki Basin, New Zealand, *Mendeley Data, v1*, https://data.mendeley.com/datasets/69xt9f4srh/draft?a=b38839ec-64c1-4ac8-a53e-51e04dbee39a. Doi: 10.17632/69xt9f4srh.1

Tables

Table 1: Stress indicators from the analysed resistivity borehole images. Azimuth: Interpreted orientation of S_{Hmax}. Depth: the mean between top and bottom stress indicator. Quality: quality ranking following the World Stress Map guidelines (Heidbach et al., 2016). Date: date of the tool run (YearMonthDay). n: number of recognised feature pairs (borehole breakouts, BO; or drilling-induced tensile fractures, DITF) in a single borehole, or section of borehole. S.D.: Standard deviation calculated according to the circular statistics of bi-polar data by Mardia (1972) with a weighting depending of the length of the feature. Length: The cumulative length of the fractured borehole sections. Top and Bottom: The depth of the uppermost and lowermost stress indicator found in the borehole. Top log and bottom log: top and bottom of the imaged interval. All depths indicated in metres, true vertical depth below mean sea level.

3-D stresses on faults in the southern Taranaki Basin, New Zealand

Borehole ID	Latitude	Longitude	Azimuth (°)	Feature Type	Depth [km]	Quality	Location	Date	n	S. D. (°)	Length [m]	Top [m]	Bottom [m]	Top log [m]	Bottom log [m]
Maari-1	-39.9677803	173.3026013	30	BO	1.73	A	Maari-Manaia	19981113	77	7.7	101.7	1297	2160	1245	2160
Maari-1	-39.9677803	173.3026013	35.1	DITF	2.08	D	Maari-Manaia	19981113	5	14.9	0.4	2062	2106	1245	2160
Maari-1 shallow	-39.9677803	173.3026013	23.9	BO	1.41	C	Maari-Manaia	19981113	40	7.3	38.4	1297	1515	1245	1515
Maari-1 shallow	-39.9677803	173.3026013		DITF			Maari-Manaia	19981113	0					1245	1515
Maari-1 deep	-39.9677803	173.3026013	33.6	BO	2.07	B	Maari-Manaia	19981113	37	5.4	63.3	1990	2160	1980	2160
Maari-1 deep	-39.9677803	173.3026013	37.8	DITF	2.08	D	Maari-Manaia	19981113	4	12.5	3.5	2062	2106	1980	2160
Maari-2	-39.9789551	173.3026799	38.9	BO	1.11	B	Maari-Manaia	20030118	91	9.2	96.5	769	1452	760	1452
Maari-2	-39.9789551	173.3026799		DITF			Maari-Manaia	20030118	0					760	1452
Matuku1	-39.6135194	173.0571222	75.9	BO	4.29	C	Tui	20140124	44	5.8	22.5	3910	4671	3600	4680
Matuku1	-39.6135194	173.0571222	82.8	DITF	3.90	D	Tui	20140124	9	5.9	5	3609	4193	3600	4680
Whio-1	-40.0173567	173.3274556	70.4	BO	1.92	A	Maari-Manaia	20140825	110	11.1	257.8	1218	2625	1080	2614

Table 2: Equations used to estimate UCS from acoustic compressional wave slowness logs. UCS in MPa; Vp in km/sec; Δtc in μs/ft

Lithology and region where developed	Equation	Reference	Lithology or Formation, this study
Bowen Basin, Australia. Fine grained, both consolidated and unconsolidated sandstones with all porosity range	UCS = 1200 exp(-0.036 Δtc)	McNally (1987)	sandstone
Globally	UCS = 1.35 (304.8 / Δtc)$^{2.6}$	Chang et al. (2006)	mudstone
unknown	UCS = 1.7 Vp$^{2.6}$	GMI (2010)	Turi and Mangahewa Formations

Figure Captions

Figure 1: Classification scheme for relative stress magnitudes and faulting style in a) normal, b) mixed normal/strike-slip, and c) strike-slip faulting systems (Anderson, 1905). Assuming that one principal stress is vertical, the ratio of maximum horizontal stress (S_{Hmax}) to vertical stress (S_v) indicates the stress regime. The depicted faults have the highest values of slip tendency (Morris et al. 1996) in each of the stress regimes: dipping 60° and striking parallel to S_{Hmax} for normal faulting stress regime; vertical and 30° either part of S_{Hmax} for strike-slip stress regime; and mixed for the normal/strike-slip regime. d) Stress rotation near a weak fault or fracture zone (after Fossen, 2016).

Figure 2**:** Regional S_{Hmax} azimuth orientations for the southern Taranaki Basin. The Eastern Mobile Belt represents the western limit of deformation associated with the oblique westward subduction of the Pacific (PAC) plate beneath the Australian (AUS) plate at southward decreasing rates of 47 – 42 mm/yr along the Hikurangi Margin (~43 mm/yr at -40°S) (King and Thrasher, 1996; Beavan et al., 2002). Inversion structures developed during the Neogene within the Eastern Mobile Belt contain most of New Zealand's producing oil and gas fields (NZPAM, 2018). Stress data are from Heidbach et al. (2018), summarised for the Taranaki region by Rajabi et al. (2016). Lines represent the S_{Hmax} azimuth with the length proportional to quality ranks A, B or C (as defined following world stress map guidelines; Heidbach et al., 2016). The colour coding is according to the stress regime with red indicating normal faulting (*NF*), green indicating strike slip faulting (*SS*), blue indicating thrust/reverse faulting (*TF*), and black for unknown regimes.

Figure 3: Fault map of the southern Taranaki Basin study area (see Fig. 2 for location) and borehole stress data. Faults (black lines and polygons) at base Oligocene time horizon mapped predominantly in 3D seismic reflection surveys (grey polygons) show hydrocarbon accumulations (NZP&M, 2018) in association with dominant N-S to NE-SW structural trends. Named boreholes have S_{hmin} magnitude information available, either leak-off test (LOT) (red filled circles), formation integrity test (FIT) (red outlined circles), or both (half-filled red circles). Side panel shows stress orientation and regime interpreted from boreholes. S_{Hmax} azimuths in boreholes Kopuwai-1, Amokura-1, Maui-5, MB-P(8) and Moki-1 are from Rajabi et al. (2016), quality ranks A to D. S_{Hmax} azimuths and stress regimes in boreholes Matuku-1, Maari-1, Maari-2 and Whio-1 are from this study.

Figure 4: a) Borehole breakout on a resistivity image log (white rectangles) and other wireline log in borehole Whio-1, defined from a blurry appearance and low resistivity on the FMI log; and difference between pairs of caliper arms (C13, C24, shaded in blue). The breakout is confined within a moderately cemented carbonate unit, as defined by increased deep resistivity (RLA5), natural gamma ray (GR) and density (RHOZ), but does not show a significant change of acoustic compressional wave slowness (DTCO) and only limited variation of neutron porosity (TNPH). Note the uncertainty on breakout width because of space in-between FMI tool pads (shaded in grey). b) Diagram of a borehole cross-section showing that borehole breakouts and drilling induced tensile fractures (DITF) form in the direction of S_{hmin} and S_{Hmax}, respectively.

Figure 5: a) S_{Hmax} azimuths as a function of depth from borehole breakouts and drilling induced tensile fractures (DITF) in boreholes Maari-1, Maari-2, Whio-1 (Maari-Manaia region) and Matuku-1 (Tui region). b) Rose diagram of S_{Hmax} azimuths from borehole breakout for each borehole, and mean orientations (Table 1) displayed as an arrow. Mean orientations in borehole Maari-1 have been displayed for the upper and lower part of the borehole separately (Table 1). S_{Hmax} azimuths from borehole breakouts with one edge masked (Fig. 4) have an additional uncertainty of ~10°.

Figure 6: Fault trace map at base Pliocene unconformity generated using the Maari-3D survey in relation to measured S_{Hmax} azimuths. a) Coherency attribute (edge detect) displayed on the laterally continuous reflection surface of the base Pliocene unconformity which separates uplifted and eroded Miocene strata from onlapping Pliocene sediments. Faults are highlighted by incoherency (black lineations) between adjacent seismic traces across an otherwise coherent (white) reflection surface. b) autopick of base Pliocene unconformity. The minor displacement normal faults (typically <10 m) in proximity to the boreholes of Maari and Moki field, and Whio-1 borehole, were mapped from linear trends in amplitude, coherency and dip attributes. The white bar indicates the location of the seismic profile in Fig. 7b. c) Rose diagram of fault strike weighted by fault length; S_{Hmax} azimuths of the three boreholes of the region (this study), and the regional Taranaki Basin S_{Hmax} azimuth (Rajabi et al., 2016); and theoretical fault strike orientation ranges for Andersonian normal and strike-slip regimes assuming the regional Taranaki Basin mean S_{Hmax} azimuth (double arrows).

Figure 7: Relationship between S_{Hmax} azimuth rotations and faults in borehole Whio-1. a) S_{Hmax} azimuth rotations in borehole Whio-1 (orange arrows) over 150 m-long depth intervals. The upper rotation coincides with two borehole-scale faults and the intersection with the seismic-scale fault. b) Seismic reflection profile (IL 1442, Maari-3D) through borehole Whio-1 (see Fig. 6 for location). The fault crossing Whio-1 reaches 200 ms TWT out of this section. c) Borehole fault zone separating a mudstone (top; high natural gamma) from a sandstone (bottom; low natural gamma). The borehole-scale fault truncates mudstone bedding and is directly underlain by a fault drag of heterolithic features shown by a decrease in dip magnitude. From left to right: statically and dynamically normalised resistivity images; interpreted sinusoids representing the fault plane and sedimentary planar features; tadpole plot of interpreted planes (dot lateral position indicating dip magnitude, tail shows the dip direction); natural gamma log.

Figure 8: Stress magnitude estimates in the Maari-Maui-Tui area. a) S_{hmin} measurements from formation integrity tests (FIT) or leak-off tests (LOT), S_v, and hydrostatic pore pressure (P_p). S_{hmin} and S_v are coloured by region (defined on Fig. 3). b) S_{hmin}, S_v, and estimates of S_{Hmax} (most likely value and possible range based on velocity log to UCS conversion) in boreholes Maari-1, Maari-2, Matuku-1 and Whio-1. The inserted block diagram represents normal and strike-slip faults consistent with the stress configurations derived from borehole data of the Maari-Manaia region. S_{hmin} and S_{Hmax} at frictional limit (equation 7) are plotted in grey. c) S_{Hmax}:S_v ratio as a function of depth for the four borehole. Grey dotted lines show the S_{hmin} magnitude at frictional limit for Matuku-1, and S_{Hmax}:S_v ratio of 1 marking the limit between normal and strike-slip stress regimes.

Figure 9: Slip tendency (Ts) for the Cape Egmont Fault (see Fig. 3 for location), the NE-SW striking fault near Maari-1 and Maari-2 boreholes (Maari Fault) and the fault intersecting borehole Whio-1 (Whio Fault) (see Fig. 6 for location), with four scenarios compatible with stress magnitudes and orientations derived from borehole data in this study. a) Normal faulting with S_{Hmax}:S_v=0.9 and S_{Hmax} azimuth 070°. b) Strike-slip regime with S_{Hmax}:S_v=1.1 and S_{Hmax} azimuth 070°; c) Strike-slip regime with S_{Hmax}:S_v=1.1 and S_{Hmax} azimuth 050°. d) Strike-slip regime with S_{Hmax}:S_v=1.5 and S_{Hmax} azimuth 070°. Each panel presents from left to right: the mohr circles (shear (τ) versus effective normal stress σ(n)); slip tendency coloured onto a stereoplot, with the envelope of the pole to planes to the three faults; slip tendency mapped onto the three faults. Stress values of the Mohr circles represent depths of 2 km; the shape of the Mohr circle does not change with increasing depth with the assumptions used.

Figure A.1: Calculation of S_v. a) Density profiles. B) S_v magnitude profiles

Figure A.2: Estimation of S_{Hmax} magnitude for the four study wells. From left to right: natural gamma ray (GR), acoustic compressional slowness (Δtc), UCS derived from Δtc (Table 2) using the McNally

equation for sandstones, Global equation for mudstones, and GMI equation for the Turi and Mangahewa Formations in borehole Whio-1; borehole breakout width; and S_{Hmax} magnitude (most likely value based on the UCS of the dominant lithology and error bars or the extreme values of UCS).

References

Anderson, E. M. (1905). The dynamics of faulting. *Transactions of the Edinburgh Geological Society*, *8*(3), 387-402. Doi: 10.1144/transed.8.3.387.

Alt, R. C., & Zoback, M. D. (2017). In situ stress and active faulting in Oklahoma. *Bulletin of the Seismological Society of America*, 107(1), 216–228. Doi: 10.1785/0120160156.

Armstrong, P. A., Allis, R. G., Funnell, R. H., & Chapman, D. S. (1998). Late Neogene exhumation patterns in Taranaki Basin (New Zealand): Evidence from offset porosity-depth trends. *Journal of Geophysical Research: Solid Earth*, *103*(B12), 30269-30282. Doi: 10.1029/98JB02843.

Athy, L.F. (1930). Density, porosity, and compaction of sedimentary rocks. *AAPG Bulletin, 14*(1).

Aydin, A. (2000). Fractures, faults, and hydrocarbon entrapment, migration and flow. *Marine and petroleum geology, 17*(7), 797-814. Doi: 10.1016/S0264-8172(00)00020-9.

Barton, C. A., Zoback, M. D., & Burns, K. L. (1988). In-situ stress orientation and magnitude at the Fenton Geothermal Site, New Mexico, determined from wellbore breakouts. *Geophysical Research Letters*, *15*(5), 467-470. Doi: 10.1029/GL015i005p00467.

Barton, C. A., & Zoback, M. D. (1994). Stress perturbations associated with active faults penetrated by boreholes: Possible evidence for near-complete stress drop and a new technique for stress magnitude measurement. *Journal of Geophysical Research: Solid Earth*, *99*(B5), 9373-9390. Doi: 10.1029/93JB03359.

Barton, C. A., Zoback, M. D., & Moos, D. (1995). Fluid flow along potentially active faults in crystalline rock. *Geology*, *23*(8), 683-686. Doi: 10.1130/0091-7613(1995)023<0683:FFAPAF>2.3.CO;2.

Barton, C., Moos, D., & Tezuka, K. (2009). Geomechanical wellbore imaging: Implications for reservoir fracture permeability. *AAPG bulletin*, *93*(11), 1551-1569. Doi: 10.1306/06180909030.

Beavan, J., Tregoning, P., Bevis, M., Kato, T., & Meertens, C. (2002). Motion and rigidity of the Pacific Plate and implications for plate boundary deformation. *Journal of Geophysical Research: Solid Earth*, 107(B10), ETG 19-1-ETG 19-15. Doi: 10.1029/2001JB000282

Boulton, C., Yao, L., Faulkner, D. R., Townend, J., Toy, V. G., Sutherland, R., Ma, S. and Shimamoto, T. (2017). High-velocity frictional properties of Alpine Fault rocks: Mechanical data, microstructural analysis, and implications for rupture propagation. *Journal of Structural Geology*, 97, 71–92. Doi: 10.1016/j.jsg.2017.02.003

Byerlee, J. (1978). Friction of rocks. *Pure and Applied Geophysics*. 116 (4–5), 615–626.

Caine, J. S., Evans, J. P., & Forster, C. B. (1996). Fault zone architecture and permeability structure. *Geology*, 24(11), 1025–1028. Doi: 10.1130/0091-7613(1996)024$<$1025:FZAAPS$>$2.3.CO;2

Chang, C., Zoback, M. D., & Khaksar, A. (2006). Empirical relations between rock strength and physical properties in sedimentary rocks. *Journal of Petroleum Science and Engineering*, *51*(3-4), 223-237. Doi: 10.1016/j.petrol.2006.01.003.

Davatzes, N. C., & Hickman, S. H. (2010). Stress, fracture, and fluid-flow analysis using acoustic and electrical image logs in hot fractured granites of the Coso geothermal field, California, USA, in M. Poppelreiter, C. Garcia-Carballido and M. Kraaijveld (eds), Dipmeter and borehole image log technology: AAPG Memoir 92, pp. 259-293. Doi: 10.1306/13181288M923134

Faulkner, D. R., Jackson, C. A. L., Lunn, R. J., Schlische, R. W., Shipton, Z. K., Wibberley, C. A. J., & Withjack, M. O. (2010). A review of recent developments concerning the structure, mechanics and fluid flow properties of fault zones. *Journal of Structural Geology*, *32*(11), 1557-1575. Doi: 10.1016/j.jsg.2010.06.009.

Ferrill, D. A., & Morris, A. P. (2003). Dilational normal faults. *Journal of Structural Geology*, *25*(2), 183-196. Doi: 10.1016/S0191-8141(02)00029-9.

Ferrill, D. A., Morris, A. P., McGinnis, R. N., Smart, K. J., Wigginton, S. S., & Hill, N. J. (2017). Mechanical stratigraphy and normal faulting. *Journal of Structural Geology*, *94*, 275-302. Doi: 10.1016/j.jsg.2016.11.010.

Fossen, H. (2016). Structural geology. *Cambridge University Press*, Ed. 2.

Giba, M., Nicol, A., & Walsh, J. J. (2010). Evolution of faulting and volcanism in a back-arc basin and its implications for subduction processes. *Tectonics*, 29(4), 1–18. Doi: 10.1029/2009TC002634

GMI (2010). Te Kiri prospect geomechanical analysis, PEP 51149, Ministry of Economic Development New Zealand Unpublished Petroleum Report PR4278.

Gudmundsson, A., Fjeldskaar, I., & Brenner, S. L. (2002). Propagation pathways and fluid transport of hydrofractures in jointed and layered rocks in geothermal fields. *Journal of Volcanology and Geothermal Research*, *116*(3-4), 257-278. Doi: 10.1016/S0377-0273(02)00225-1.

Halliburton Australia Pty Ltd. (1999). Maari-1 & 1A well completion report, PPL 38413. Ministry of Economic Development New Zealand Unpublished Petroleum Report PR1572.

Heap, M.J., Faulkner, D.R., Meredith, P.G. and Vinciguerra, S., 2010. Elastic moduli evolution and accompanying stress changes with increasing crack damage: implications for stress changes around fault zones and volcanoes during deformation. *Geophysical Journal International*, 183(1), pp.225-236. Doi: 10.1111/j.1365-246X.2010.04726.x

Heidbach, O., Müller, B., Reinecker, J., Stephansson, O., Tingay, M., & Zang, A. (2016). WSM quality ranking scheme, database description and analysis guidelines for stress indicator. World Stress Map. Doi: 10.1029/2001GC000252.

Heidbach, O., Rajabi, M., Cui, X., Fuchs, K., Müller, B., Reinecker, J., Reiter, K., Tingay, M., Wenzel, F., Xie, F., Ziegler, M.O., M.-L. Zoback, & Zoback, M. (2018). The World Stress Map database release 2016: Crustal stress pattern across scales. *Tectonophysics, 744*, 484-498. Doi: doi.org/10.1016/j.tecto.2018.07.007.

Hemmings-Sykes, S. (2012). The influence of faulting on hydrocarbon migration in the Kupe area, South Taranaki Basin, New Zealand, Unpubl. Msc thesis, Victoria University of Wellington.

Hickman, S., & Zoback, M. (2004). Stress orientations and magnitudes in the SAFOD pilot hole. *Geophysical Research Letters*, *31*(15). Doi: 10.1029/2004GL020043.

Horan, S. (1997). Borehole stress study of the Kupe South and Toru fields: Ministry of Energy Petroleum Report PR2764.

Ilg, B. R., Hemmings-Sykes, S., Nicol, A., Baur, J., Fohrmann, M., Funnell, R., & Milner, M. (2012). Normal faults and gas migration in an active plate boundary, southern Taranaki Basin, offshore New Zealand. *AAPG bulletin*, *96*(9), 1733-1756.

Jaeger, J. C., Cook, N. G., & Zimmerman, R. (2009). *Fundamentals of rock mechanics*. John Wiley & Sons.

Jolie, E., Klinkmueller, M., Moeck, I., & Bruhn, D. (2016). Linking gas fluxes at Earth's surface with fracture zones in an active geothermal field. *Geology*, *44*(3), 187-190. Doi: 10.1130/G37412.1.

King, P.R., Thrasher, G.P. (1996). Cretaceous Cenozoic geology and petroleum systems of the Taranaki Basin, New Zealand. Institute of Geological & Nuclear Sciences monograph 13. Lower Hutt, New Zealand: Institute of Geological & Nuclear Sciences. 243 p

Manzocchi, T., Childs, C., & Walsh, J. J. (2010). Faults and fault properties in hydrocarbon flow models. *Geofluids*, *10*(1-2), 94-113. Doi: 10.1111/j.1468-8123.2010.00283.x.

Mardia, K. V. (1972). Statistics of Directional Data: Probability and Mathematical Statistics, Academic Press, London.

McNally, G. H. (1987). Estimation of coal measures rock strength using sonic and neutron logs. *Geoexploration*, *24*(4-5), 381-395. Doi: 10.1016/0016-7142(87)90008-1.

McNamara, D. D., Massiot, C., Lewis, B., & Wallis, I. C. (2015). Heterogeneity of structure and stress in the Rotokawa Geothermal Field, New Zealand. *Journal of Geophysical Research: Solid Earth*, *120*(2), 1243-1262. Doi: 10.1002/2014JB011480.

Mildren, S. and Meyer, J. (2006). Moana Prospect: Cross-Fault Pressure Difference Analysis. Northern Taranaki Graben, New Zealand. Ministry of Economic Development New Zealand Unpublished Petroleum Report PR3647.

Mildren, S., Meyer, J. and Hillis, R.(2001). Pohokura ERD wellbore stability study. Ministry of Economic Development New Zealand Unpublished Petroleum Report PR2651.

Morris, A., Ferrill, D. A., & Henderson, D. B. (1996). Slip-tendency analysis and fault reactivation. *Geology*, *24*(3), 275-278. Doi: 10.1130/0091-7613(1996)024<0275:STAAFR>2.3.CO;2.

Morris, A. P., & Ferrill, D. A. (2009). The importance of the effective intermediate principal stress (σ' 2) to fault slip patterns. *Journal of Structural Geology*, *31*(9), 950-959. Doi: 10.1016/j.jsg.2008.03.013

Mouslopoulou, V., Nicol, A., Walsh, J.J., Begg, J.G., Townsend, D.B. & Hristopulos, D.T. (2012). Fault-slip accumulation in an active rift over thousands to millions of years and the importance of paleoearthquake sampling. *Journal of Structural Geology, 36*, pp.71-80. Doi: 10.1016/j.jsg.2011.11.010.

Nafe, J. E., & Drake, C. L. (1957). Variation with depth in shallow and deep water marine sediments of porosity, density and the velocities of compressional and shear waves. *Geophysics*, *22*(3), 523-552. Doi: 10.1190/1.1438386.

New Zealand Petroleum & Minerals (NZP&M) (2018) https://www.nzpam.govt.nz/maps-geoscience/petroleum-datapack/. Accessed 17 October, 2018.

New Zealand Ministry of Business, Innovation and Employment (2018). https://www.mbie.govt.nz/info-services/sectors-industries/energy/energy-data-modelling/publications/petroleum-reserves-data . Accessed 17 October 2018.

Nicol, A., Walsh, J., Berryman, K., & Nodder, S. (2005). Growth of a normal fault by the accumulation of slip over millions of years. Journal of Structural Geology, 27(2), 327–342. Doi: 10.1016/j.jsg.2004.09.002

Nicol, A., Seebeck, H., Field, B., McNamara, D., Childs, C., Craig, J., & Rolland, A. (2017). Fault permeability and CO2 storage. *Energy Procedia*, *114*, 3229-3236. Doi: 10.1016/j.egypro.2017.03.1454.

Nodder, S. D. (1993). Neotectonics of the offshore Cape Egmont Fault Zone, Taranaki Basin, New Zealand. *New Zealand journal of geology and geophysics*, *36*(2), 167-184. Doi: 10.1080/00288306.1993.9514566.

OMV New Zealand Limited (2003). Maari-2 well completion report, Ministry of Economic Development New Zealand Unpublished Petroleum Report PR2772.

Rajabi, M., Ziegler, M., Tingay, M., Heidbach, O., & Reynolds, S. (2016). Contemporary tectonic stress pattern of the Taranaki Basin, New Zealand. *Journal of Geophysical Research: Solid Earth*, *121*(8), 6053-6070. Doi: 10.1002/2016JB013178.

Rajabi, M., Tingay, M., King, R. and Heidbach, O., 2017a. Present-day stress orientation in the Clarence-Moreton Basin of New South Wales, Australia: a new high density dataset reveals local stress rotations. *Basin Research*, 29, pp.622-640. Doi: 10.1111/bre.12175

Rajabi, M., Heidbach, O., Tingay, M. and Reiter, K., 2017b. Prediction of the present-day stress field in the Australian continental crust using 3D geomechanical–numerical models. *Australian Journal of Earth Sciences*, 64(4), pp.435-454. doi: 10.1080/08120099.2017.1294109

Reilly, C., Nicol, A., Walsh, J. J., & Seebeck, H. (2015). Evolution of faulting and plate boundary deformation in the Southern Taranaki Basin, New Zealand. *Tectonophysics*, 651, 1–18. Doi: 10.1016/j.tecto.2015.02.009

Reilly, C., Nicol, A., Walsh, J. J., & Kroeger, K. F. (2016). Temporal changes of fault seal and early charge of the Maui Gas-condensate field, Taranaki Basin, New Zealand. *Marine and Petroleum Geology*, *70*, 237-250. Doi: 10.1016/j.marpetgeo.2015.11.018.

Rice, J. R. (1992). Fault stress states, pore pressure distributions, and the weakness of the San Andreas fault. In *International geophysics* (Vol. 51, pp. 475-503). Academic Press. Doi: 10.1016/S0074-6142(08)62835-1.

Rinaldi, A. P., Rutqvist, J., & Cappa, F. (2014). Geomechanical effects on CO_2 leakage through fault zones during large-scale underground injection. *International Journal of Greenhouse Gas Control*, 20, 117–131. Doi: 10.1016/j.ijggc.2013.11.001

Roncaglia, L., Fohrmann, M., Milner, M., Morgans, H.E.G., & Crundwell, M.P. (2013). Well log stratigraphy in the central and southern offshore area of the Taranaki Basin, New Zealand. *GNS Science report 2013/27*. Accessible at http://shop.gns.cri.nz/sr_2013-027-pdf

Seebeck, H. C., Nicol, A., Walsh, J. J., Childs, C., Beetham, R. D., & Pettinga, J. (2014a). Fluid flow in fault zones from an active rift. *Journal of Structural Geology*, 62, 52–64. Doi:10.1016/j.jsg.2014.01.008

Seebeck, H. C., Nicol, A., Giba, M., Pettinga, J., & Walsh, J. J. (2014b). Geometry of the subducting Pacific plate since 20 Ma, Hikurangi margin, New Zealand. *Journal of the Geological Society*, 171(1), 131–143. Doi: 10.1144/jgs2012-145Sherburn, S., & White, R. S. (2006). Tectonics of the Taranaki

region, New Zealand: earthquake focal mechanisms and stress axes. *New Zealand journal of geology and geophysics*, *49*(2), 269-279. Doi: 10.1080/00288306.2006.9515165.

Shell Todd Oil Services Ltd, 2002. Rock strength on core samples From Wells Pohokura-1 and Pohokura-2, Ministry of Economic Development New Zealand Unpublished Petroleum Report PR2778.

Sibson, R.H. (1994). Crustal stress, faulting and fluid flow. *Geological Society, London, Special Publications*, 78(1), pp.69-84. Doi: 10.1144/GSL.SP.1994.078.01.07

Sibson, R.H., 1990. Rupture nucleation on unfavourably oriented faults. *Bulletin of the Seismological Society of America* 80, 1604–2580.

Sykes, R. (2012). NZ Petroleum PVT Database. GNS v1., Ministry of Economic Development New Zealand Unpublished Petroleum Report PR4519.

Sperner, B., Müller, B., Heidbach, O., Delvaux, D., Reinecker, J., & Fuchs, K. (2003). Tectonic stress in the Earth's crust: Advances in the World Stress Map project. *Geological Society, London, Special Publications*, *212*(1), 101-116. Doi: 10.1144/GSL.SP.2003.212.01.07.

Stagpoole, V., and A. Nicol (2008). Regional structure and kinematic history of a large subduction back thrust: Taranaki Fault, New Zealand. *Journal of Geophysical Research*, *113*(B01403). doi:10.1029/2007JB005170

Strogen, D. P., Seebeck, H., Nicol, A., & King, P. R. (2017). Two-phase Cretaceous–Paleocene rifting in the Taranaki Basin region, New Zealand; implications for Gondwana break-up. *Journal of the Geological Society*, 174(5), 929-946. Doi: 10.1144/jgs2016-160

Thrasher, G., Seebeck, H., Viskovic, P., Bull, S., Sarma, M., & Kroeger, K. (2018). Time structure grids for the greater Maui-Maari-Tui region, Taranaki Basin, New Zealand, GNS Science Data Series 25a. 11p, 1 DVD. Available at: https://data.gns.cri.nz/pbe/Content/outputs/DS25a/Report/navigation/index.html

Tingay, M., Morley, C. K., Hillis, R., & Meyer, J. (2010). Present-day stress orientation in Thailand's basins. *Journal of Structural Geology*, 32, 235–248. Doi: 10.1016/j.jsg.2009.11.008

Townend, J., & Zoback, M. D. (2000). How faulting keeps the crust strong. *Geology*, *28*(5), 399-402. Doi: 10.1130/0091-7613(2000)28<399:HFKTCS>2.0.CO;2.

Townend, J., Sherburn, S., Arnold, R., Boese, C., & Woods, L. (2012). Three-dimensional variations in present-day tectonic stress along the Australia–Pacific plate boundary in New Zealand. *Earth and Planetary Science Letters*, *353*, 47-59. Doi: 10.1016/j.epsl.2012.08.003

Townsend, D., Vonk, A.J., & Kamp, P.J.J. (2008). Geology of the Taranaki area: scale 1:250,000 geological map. *Lower Hutt: GNS Science. Institute of Geological & Nuclear Sciences 1:250,000 geological map 7*. 77 p.+1 folded map.

Townsend, D., Nicol, A., Mouslopoulou, V., Begg, J.G., Beetham, R.D., Clark, D., Giba, M., Heron, D., Lukovic, B., McPherson, A. & Seebeck, H. (2010). Palaeoearthquake histories across a normal fault system in the southwest Taranaki Peninsula, New Zealand. *New Zealand Journal of Geology and Geophysics, 53*(4), pp.375-394.

Turner, J.P. & Williams, G.A. 2004. Sedimentary basin inversion and intra-plate shortening. *Earth-Science Reviews*, 65, 277–304. doi:10.1016/j.earscirev.2003.10.002

Valley, B., & Evans, K. F. (2019). Stress magnitudes in the Basel enhanced geothermal system. *International Journal of Rock Mechanics and Mining Sciences*, 118. Doi: 10.1016/j.ijrmms.2019.03.008. .

Viskovic, P., Thrasher, G., Seebeck, H., Bull, S., Sarma, M., & Kroeger, K. (2019). Time and Depth structure grids and velocity model of the greater Maui-Maari-Tui region, Taranaki Basin, New Zealand, *GNS Science Data Series 25b*. 23p. Available at: https://data.gns.cri.nz/pbe/Content/outputs/DS25b/Report/navigation/index.html

Wallace, L., Beavan, R. J., McCaffrey, R., & Darby, D. J. (2004). Subduction zone coupling and tectonic block rotations in the North Island, New Zealand. *Journal of Geophysical Research B: Solid Earth*, 109, 1–21. Doi: 10.1029/2004JB003241

Walsh III, F. R., & Zoback, M. D. (2016). Probabilistic assessment of potential fault slip related to injection-induced earthquakes: Application to north-central Oklahoma, USA. *Geology*, *44*(12), 991-994. Doi: doi.org/10.1130/G38275.1.

Webb, T. H., & Anderson, H. (1998). Focal mechanisms of large earthquakes in the North Island of New Zealand: slip partitioning at an oblique active margin. *Geophysical Journal International*, *134*(1), 40-86. Doi: 10.1046/j.1365-246x.1998.00531.x.

Webster, M., O'Connor, S., Pindar, B., & Swarbrick, R. (2011). Overpressures in the Taranaki Basin: Distribution, causes, and implications for exploration. *AAPG bulletin*, *95*(3), 339-370.

Wiprut, D., & Zoback, M. (2000). Constraining the stress tensor in the Visund field, Norwegian North Sea: Application to wellbore stability and sand production. *International Journal of Rock Mechanics and Mining Sciences*, *37*(1-2), 317-336. Doi: 10.1016/S1365-1609(99)00109-4

Wunderlich, A. & Mayer, J. (2018). The Manaia discovery – a great surprise. In: *Proceedings of the New Zealand Petroleum Conference, Wellington, New Zealand*: Petroleum Exploration and Production Association of New Zealand.

Wyman, K. & Smith, N.(2015). PEP 51313 Whio-1 Completion Report, NZP&M, Ministry of Business, Innovation & Employment (MBIE), New Zealand Unpublished Petroleum Reports PR5207.

Yale, D. P. (2003). Fault and stress magnitude controls on variations in the orientation of in situ stress. *Geological Society, London, Special Publications*, *209*(1), 55-64. Doi: 10.1144/GSL.SP.2003.209.01.06

Zoback, M. D. (2007). Reservoir geomechanics, Cambridge University Press.

Zoback, M. D., Barton, C. A., Brudy, M., Castillo, D. A., Finkbeiner, T., Grollimund, B. R., Moos, D. B., Peska, P., Ward, C. D. & Wiprut, D. J. (2003). Determination of stress orientation and magnitude in deep wells*, International Journal of Rock Mechanics and Mining Sciences* 40(7-8), 1049-1076. Doi: 10.1016/j.ijrmms.2003.07.001

Figure 1

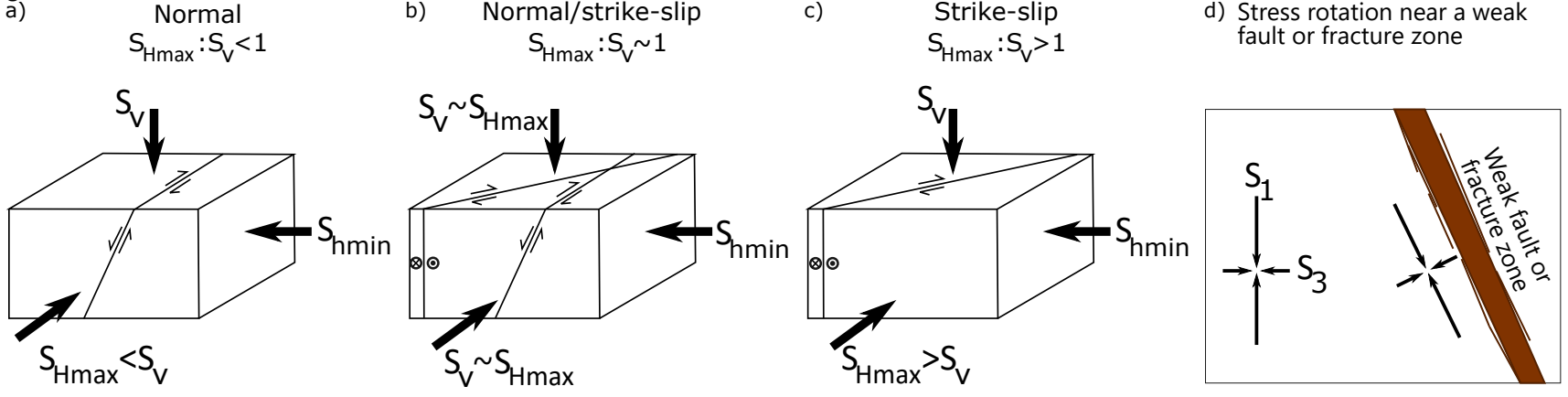
a)
Normal
$S_{Hmax}:S_V<1$
S_V
S_{hmin}
$S_{Hmax}<S_V$
b)
Normal/strike-slip
$S_{Hmax}:S_V\sim1$
$S_V\sim S_{Hmax}$
S_{hmin}
$S_V\sim S_{Hmax}$
c)
Strike-slip
$S_{Hmax}:S_V>1$
S_V
S_{hmin}
$S_{Hmax}>S_V$
d) Stress rotation near a weak fault or fracture zone
S_1
S_3
Weak fault or fracture zone

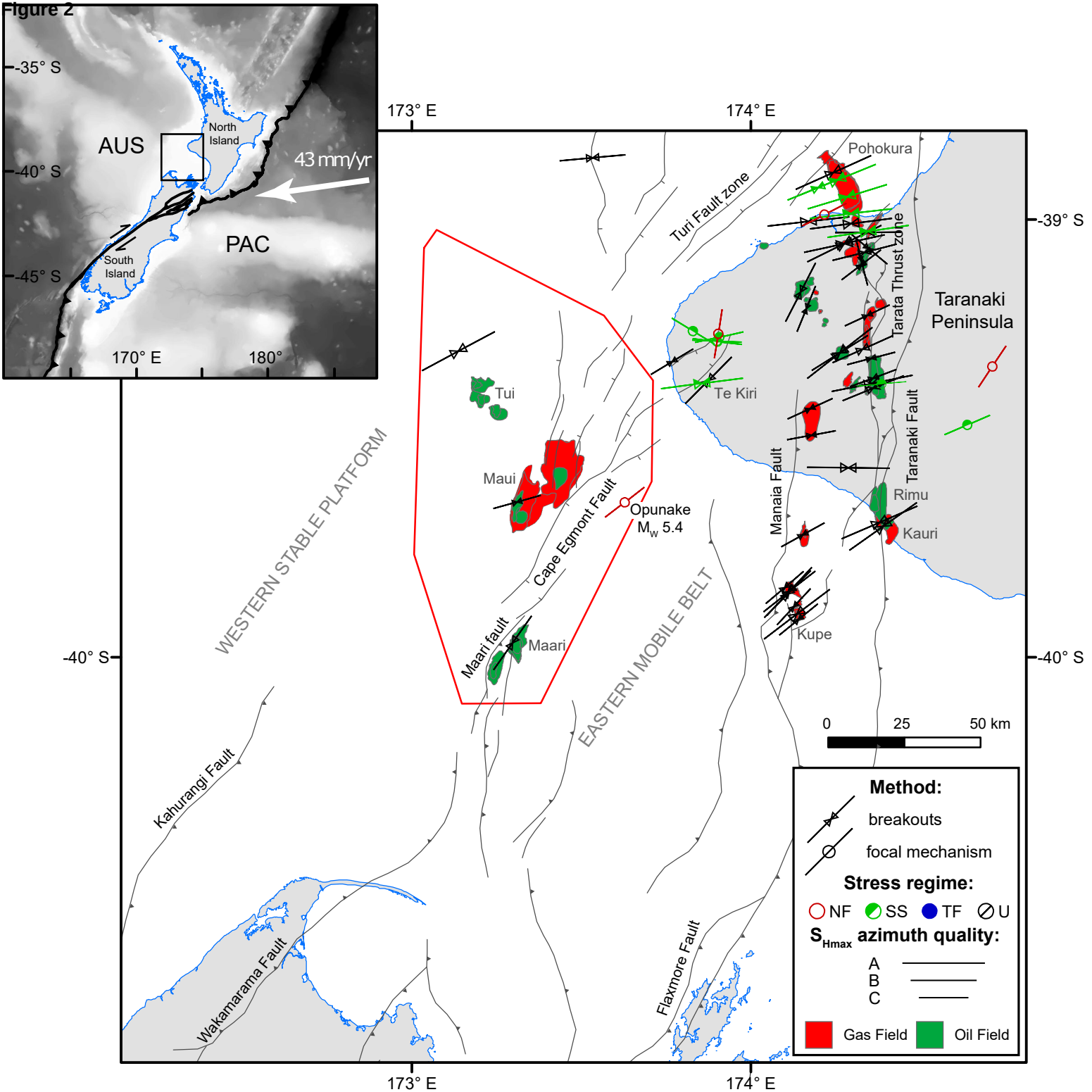
Figure 2
-35° S
-40° S
-45° S
170° E
180°
AUS
PAC
North Island
South Island
43 mm/yr
173° E
174° E
-39° S
-40° S
Pohokura
Turi Fault zone
Tarata Thrust zone
Taranaki Peninsula
Tui
Te Kiri
Maui
Cape Egmont Fault
Opunake
M_w 5.4
Manaia Fault
Taranaki Fault
Rimu
Kauri
Kupe
Maari fault
Maari
WESTERN STABLE PLATFORM
EASTERN MOBILE BELT
Kahurangi Fault
Wakamarama Fault
Flaxmore Fault
0
25
50 km
Method:
breakouts
focal mechanism
Stress regime:
NF
SS
TF
U
S_{Hmax} azimuth quality:
A
B
C
Gas Field
Oil Field

Figure 3

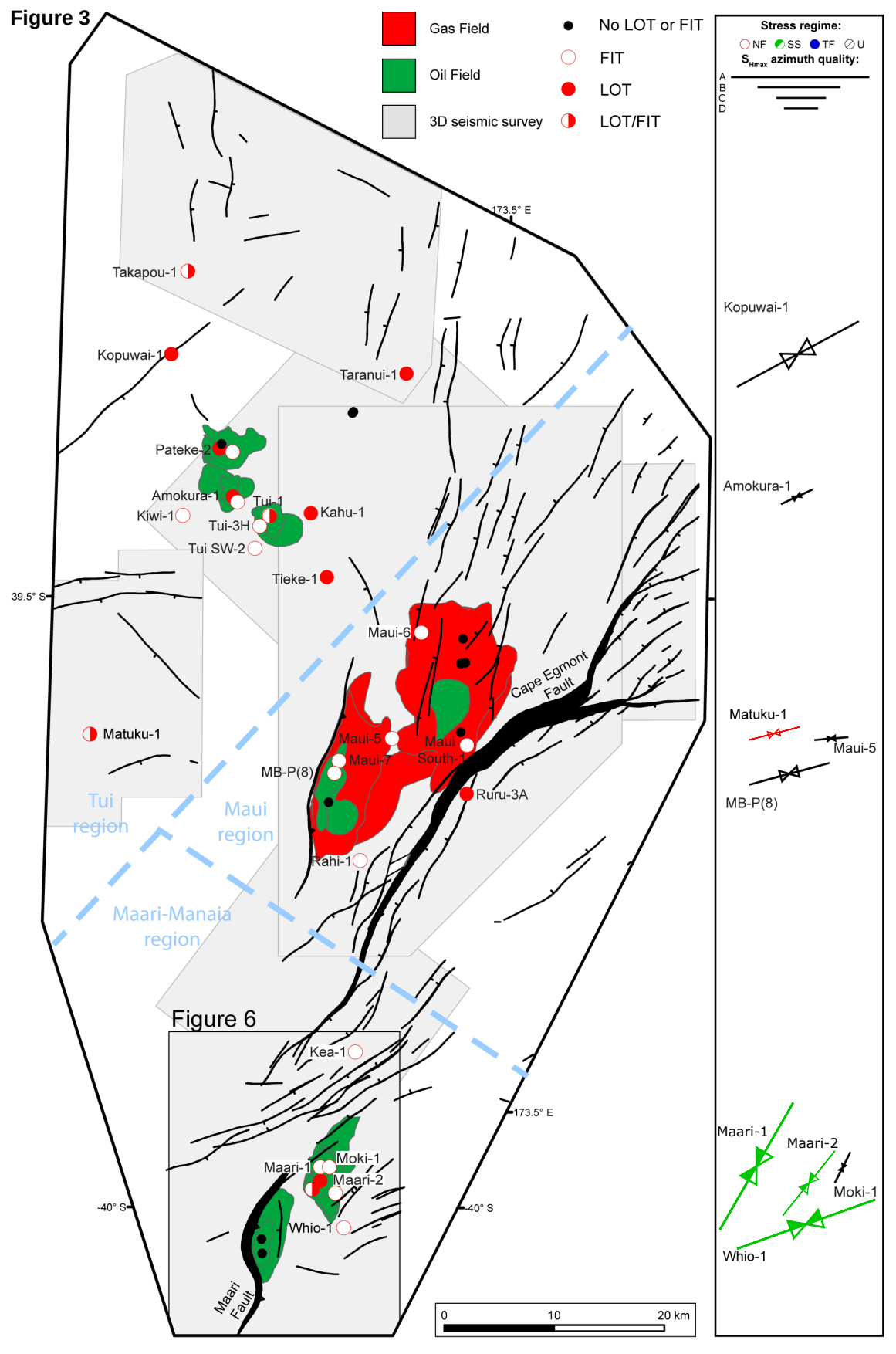
Gas Field
Oil Field
3D seismic survey
No LOT or FIT
FIT
LOT
LOT/FIT
Stress regime:
NF SS TF U
S Hmax azimuth quality:
A
B
C
D
173.5° E
39.5° S
Takapou-1
Kopuwai-1
Taranui-1
Pateke-2
Amokura-1
Kiwi-1
Tui-1
Tui-3H
Tui SW-2
Kahu-1
Tieke-1
Maui-6
Maui-5
Maui-7
Maui South-1
MB-P(8)
Cape Egmont Fault
Ruru-3A
Rahi-1
Matuku-1
Tui region
Maui region
Maari-Manaia region
Figure 6
Kea-1
Moki-1
Maari-1
Maari-2
Whio-1
Maari Fault
-40° S
0
10
20 km
Kopuwai-1
Amokura-1
Matuku-1
Maui-5
MB-P(8)
Maari-1
Maari-2
Moki-1
Whio-1

Figure 4

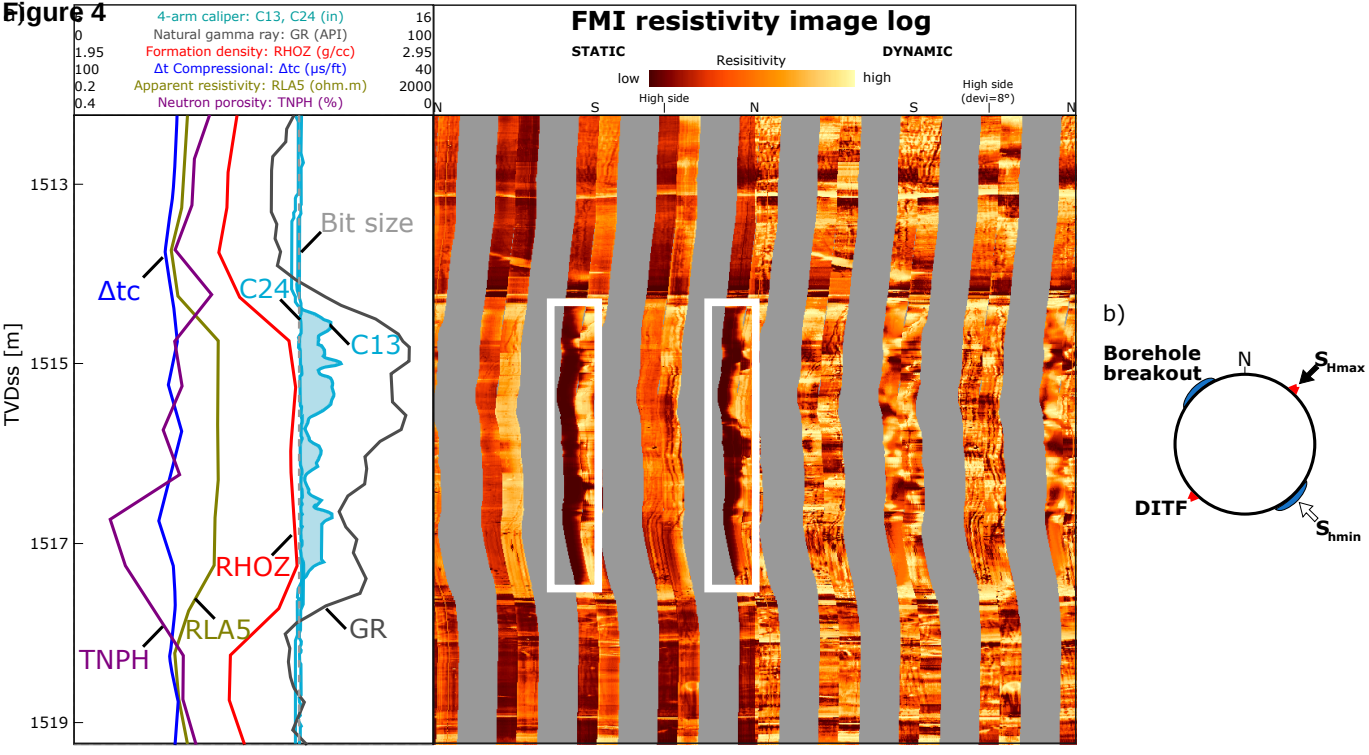
4-arm caliper: C13, C24 (in)
16
0
Natural gamma ray: GR (API)
100
1.95
Formation density: RHOZ (g/cc)
2.95
100
Δt Compressional: Δtc (μs/ft)
40
0.2
Apparent resistivity: RLA5 (ohm.m)
2000
0.4
Neutron porosity: TNPH (%)
0
FMI resistivity image log
STATIC
DYNAMIC
Resistivity
low
high
High side
High side (devi=8°)
N
S
N
S
N
TVDss [m]
1513
1515
1517
1519
Bit size
Δtc
C24
C13
RHOZ
RLA5
GR
TNPH
b)
Borehole breakout
N
S_{Hmax}
DITF
S_{hmin}

Figure 5

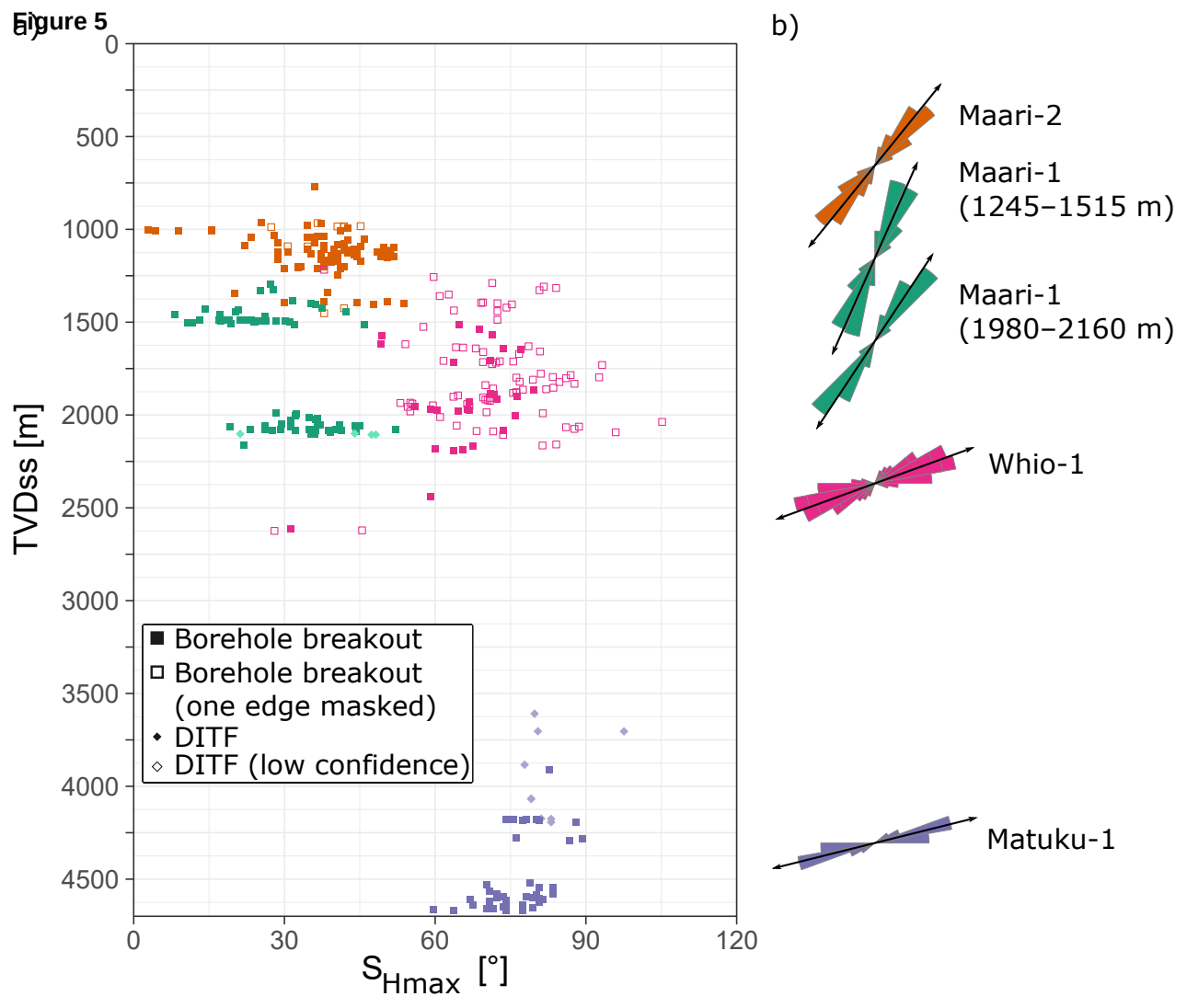
a)
b)
TVDss [m]
0
500
1000
1500
2000
2500
3000
3500
4000
4500
0
30
60
90
120
S Hmax [°]
Borehole breakout
Borehole breakout (one edge masked)
DITF
DITF (low confidence)
Maari-2
Maari-1 (1245–1515 m)
Maari-1 (1980–2160 m)
Whio-1
Matuku-1

Figure 6

a)


0 2 4 6 8 10
Km

b)

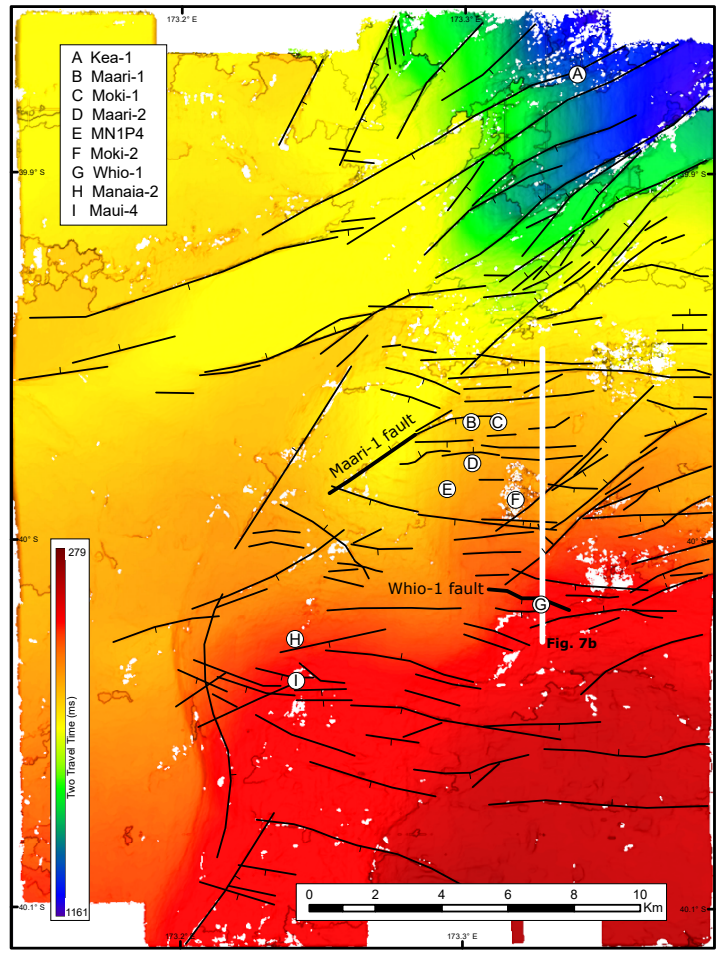
A Kea-1
B Maari-1
C Moki-1
D Maari-2
E MN1P4
F Moki-2
G Whio-1
H Manaia-2
I Maui-4
Maari-1 fault
Whio-1 fault
Fig. 7b
279
Two Travel Time (ms)
1161
0 2 4 6 8 10
Km

c)

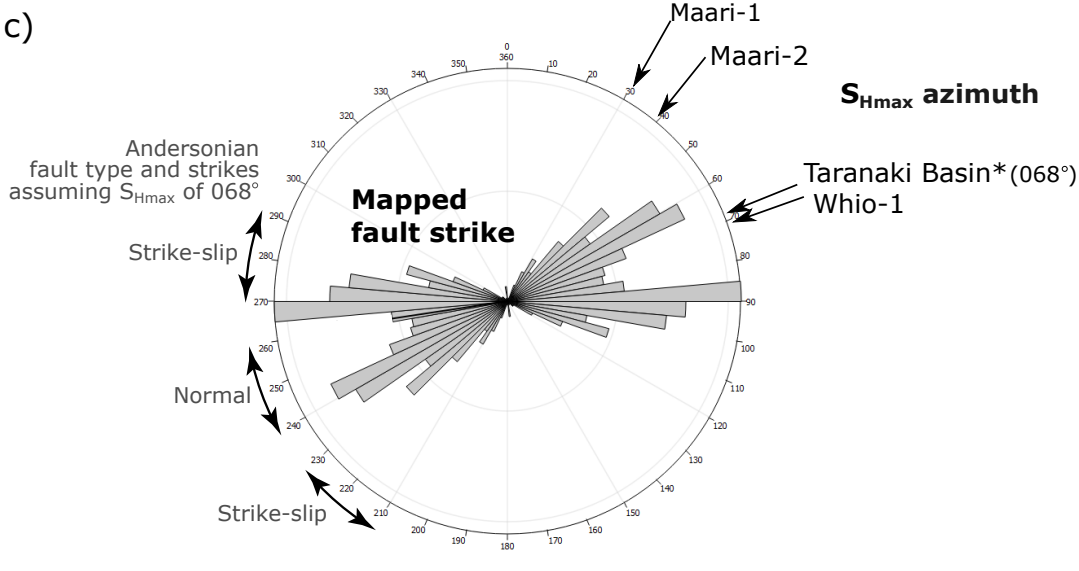
Maari-1
Maari-2
S_{Hmax} azimuth
Taranaki Basin* (068°)
Whio-1
Andersonian
fault type and strikes
assuming S_{Hmax} of 068°
Strike-slip
Normal
Strike-slip
Mapped
fault strike

Figure 7

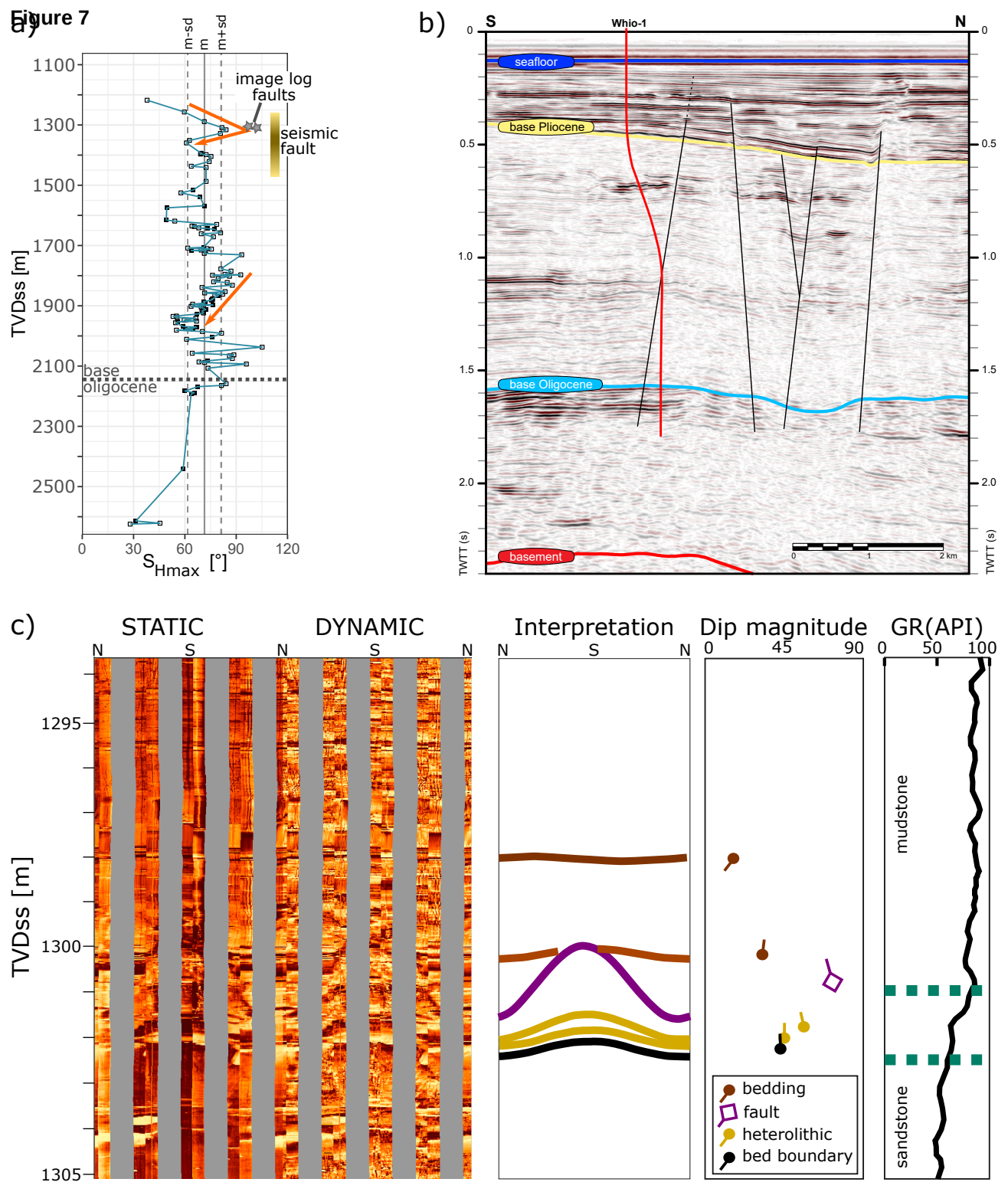
a)
m-sd
m
m+sd
image log faults
seismic fault
TVDss [m]
1100
1300
1500
1700
1900
2100
2300
2500
base oligocene
0
30
60
90
120
S Hmax [°]
b)
S
Whio-1
N
seafloor
base Pliocene
base Oligocene
basement
TWTT (s)
0
0.5
1.0
1.5
2.0
0
1
2 km
c)
STATIC
DYNAMIC
Interpretation
Dip magnitude
GR(API)
N
S
0
45
90
0
50
100
TVDss [m]
1295
1300
1305
bedding
fault
heterolithic
bed boundary
mudstone
sandstone

Figure 8

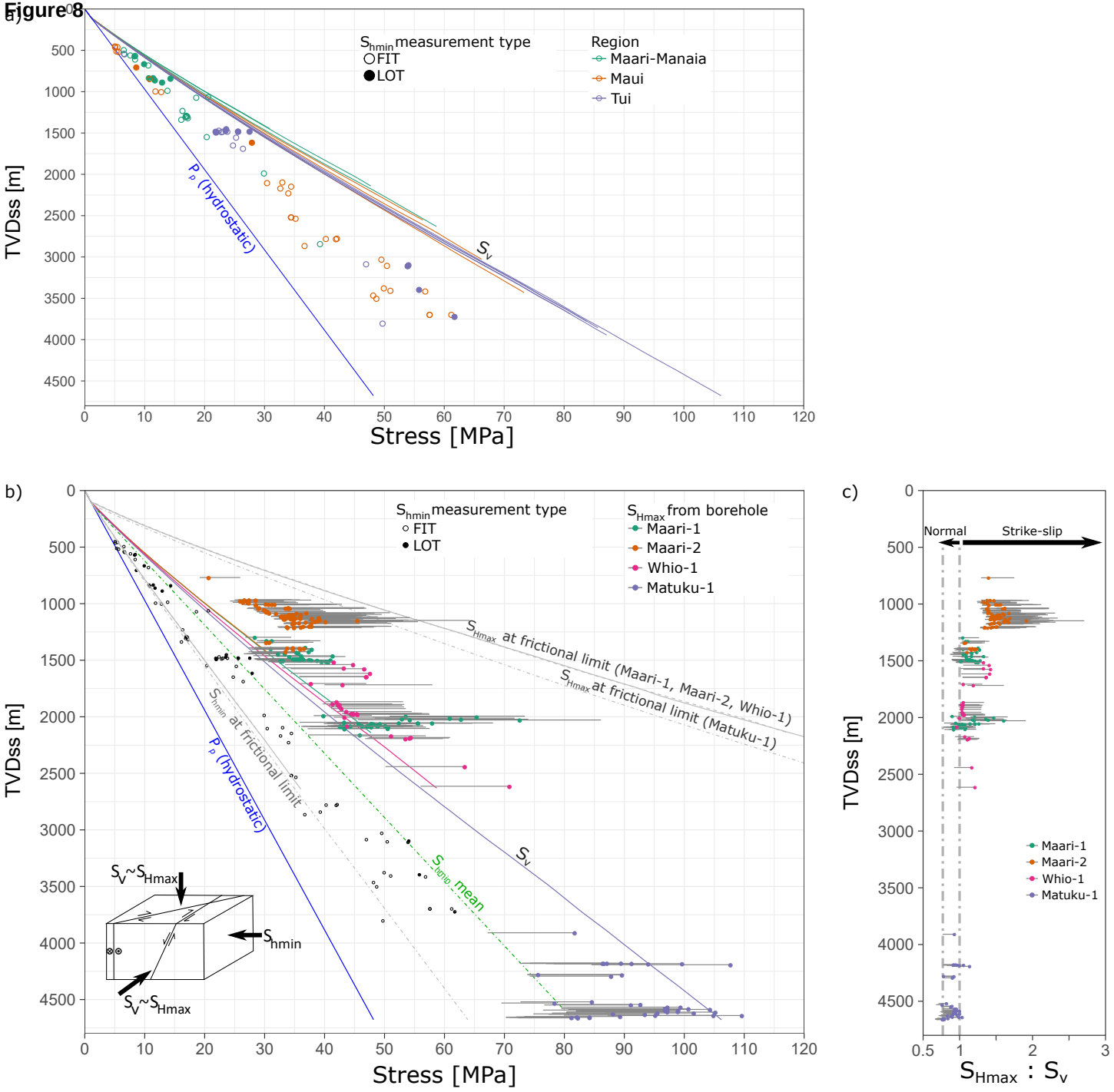
a)
TVDss [m]
Stress [MPa]
Shmin measurement type
FIT
LOT
Region
Maari-Manaia
Maui
Tui
Pp (hydrostatic)
Sv
b)
TVDss [m]
Stress [MPa]
Shmin measurement type
FIT
LOT
SHmax from borehole
Maari-1
Maari-2
Whio-1
Matuku-1
SHmax at frictional limit (Maari-1, Maari-2, Whio-1)
SHmax at frictional limit (Matuku-1)
Shmin at frictional limit
Pp (hydrostatic)
Sv
Shmin mean
SV~SHmax
Shmin
SV~SHmax
c)
TVDss [m]
Normal
Strike-slip
Maari-1
Maari-2
Whio-1
Matuku-1
SHmax : Sv

Figure 9

a) *Normal faulting regime, S_{Hmax}:S_v=0.9*
S_{Hmax} azimuth: 070°

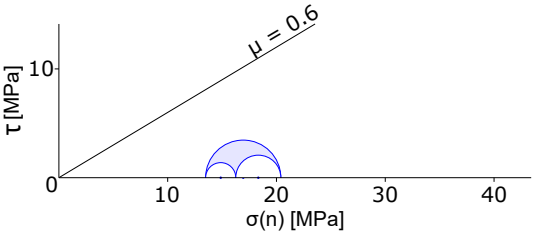

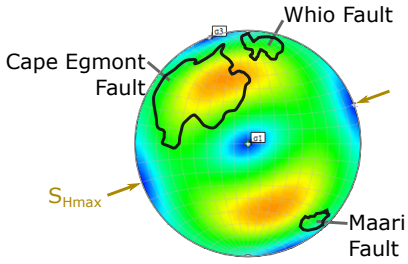

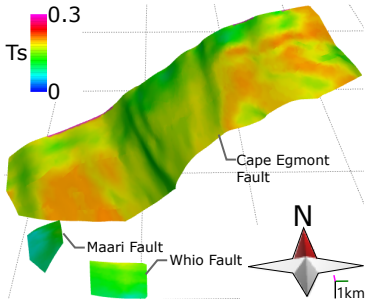

b) *Strike-slip regime, S_{Hmax}:S_v=1.1*
S_{Hmax} azimuth: 070°

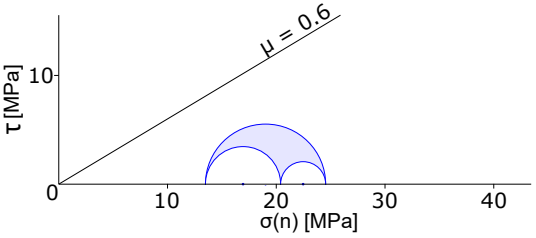

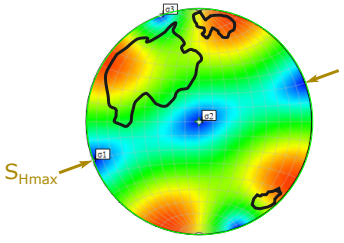

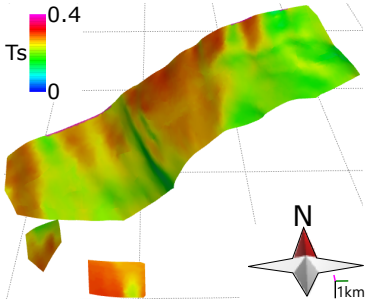

c) *Strike-slip regime, S_{Hmax}:S_v=1.1*
S_{Hmax} azimuth: 050°

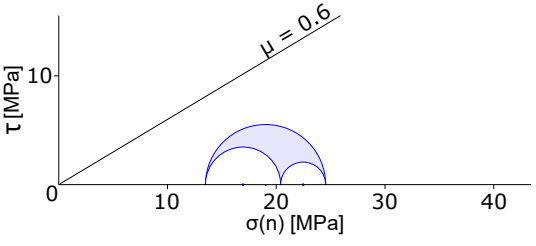

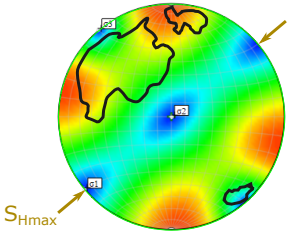

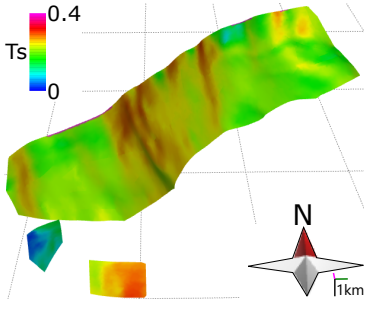

d) *Strike-slip regime, S_{Hmax}:S_v=1.5*
S_{Hmax} azimuth: 070°

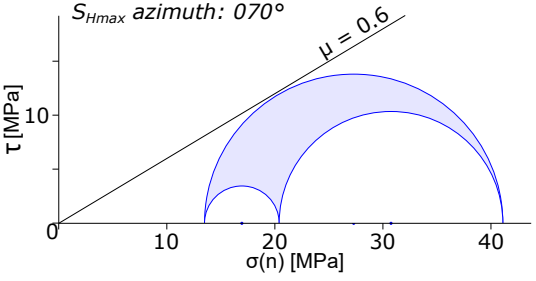

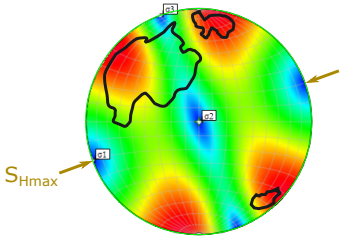

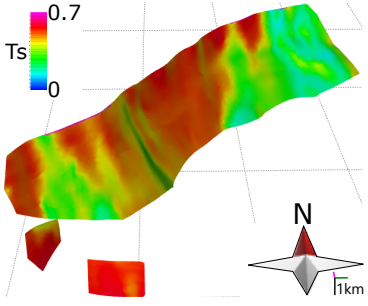

Figure A.1

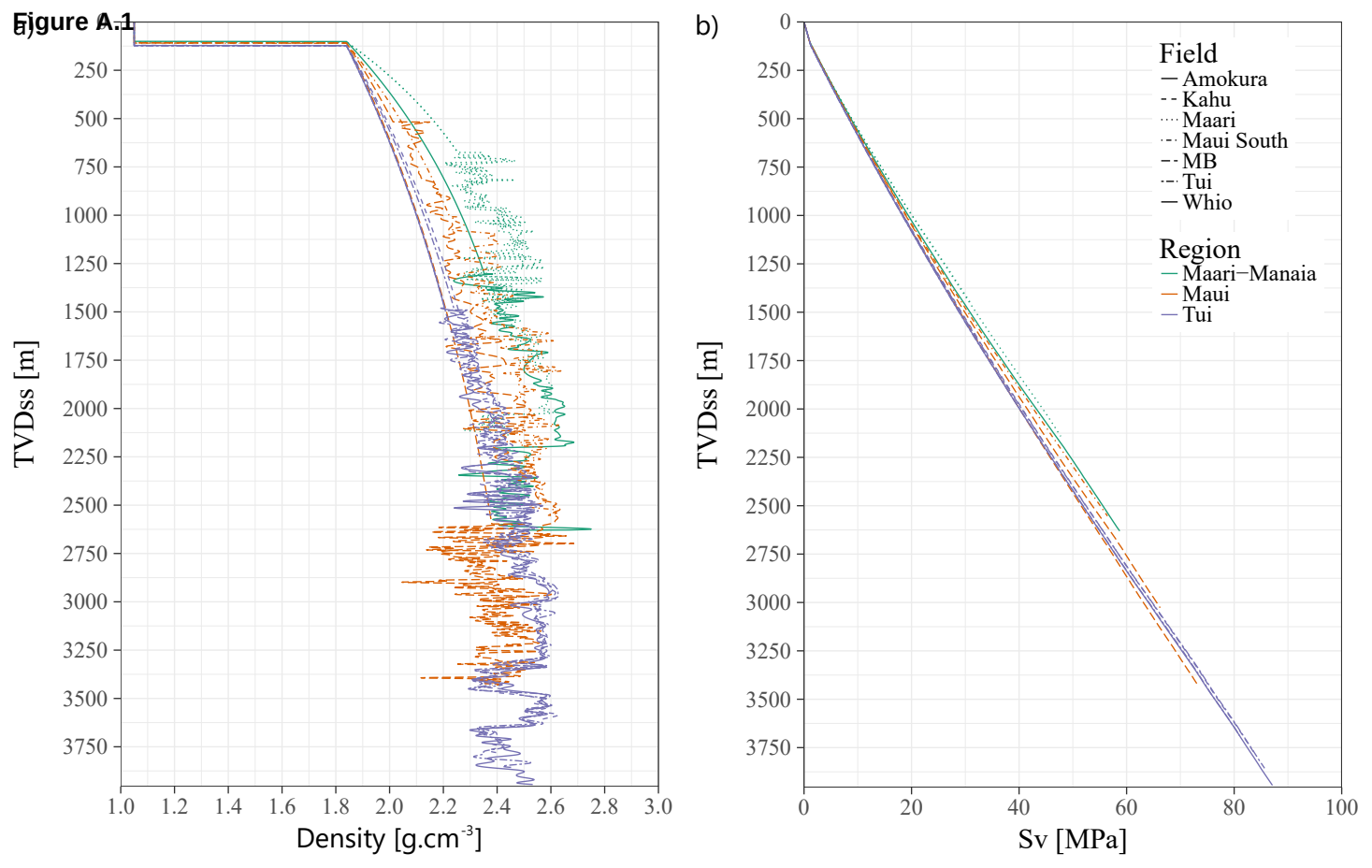
a)
b)
TVDss [m]
Density [g.cm-3]
Sv [MPa]
Field
Amokura
Kahu
Maari
Maui South
MB
Tui
Whio
Region
Maari−Manaia
Maui
Tui

Figure A.2

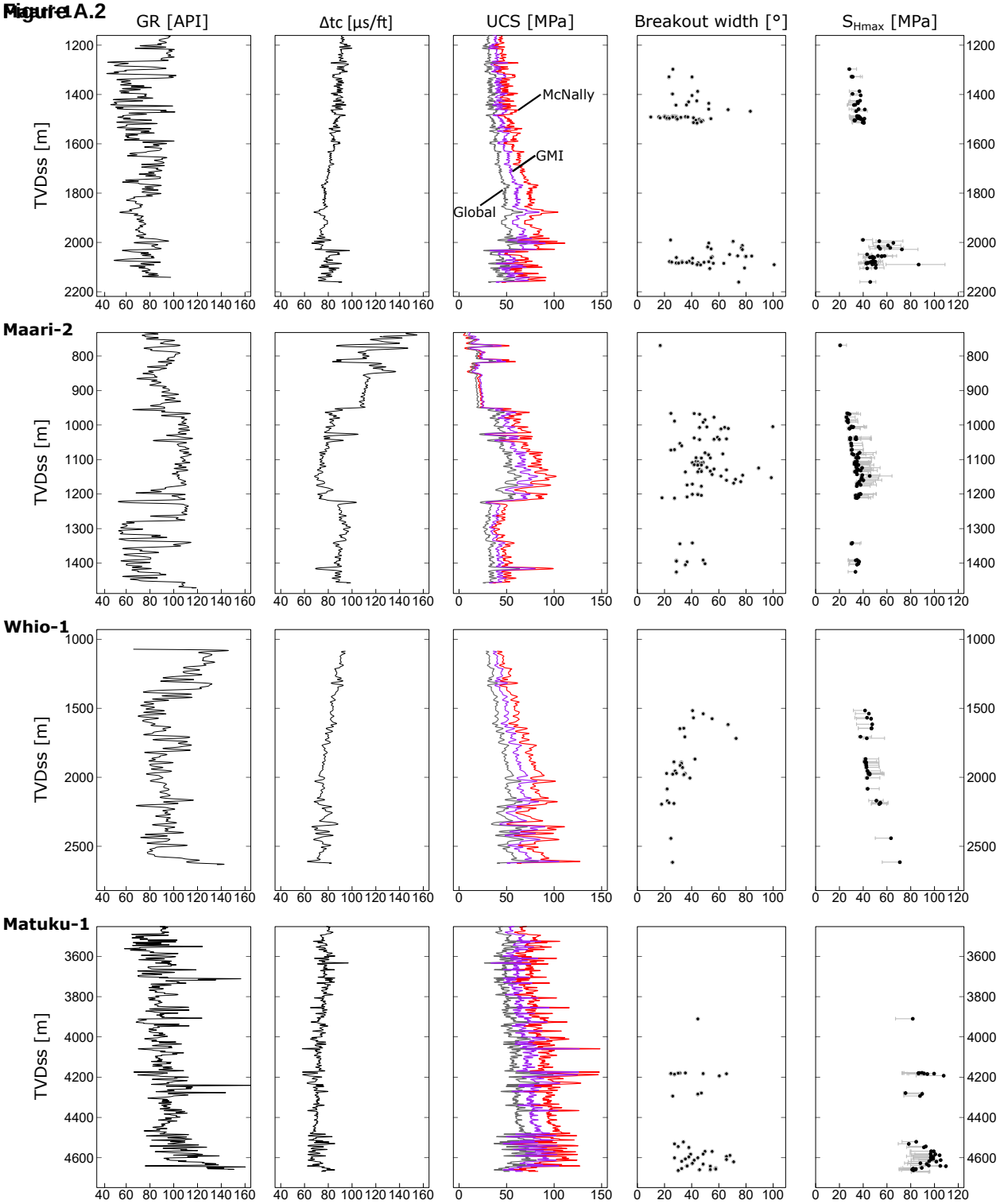
GR [API]
Δtc [μs/ft]
UCS [MPa]
Breakout width [°]
S_{Hmax} [MPa]
McNally
GMI
Global
TVDss [m]
Whio-1
Maari-2
Matuku-1